Droplet spreading, imbibition and solidification on porous media

By A. ZADRAŽIL[1], F. STEPANEK[2] AND O. K. MATAR[2]†

[1]Department of Chemical Engineering, Prague Institute of Chemical Technology,
Technická 5, 166 28 Praha 6, Czech Republic

[2]Department of Chemical Engineering, Imperial College London, South Kensington Campus,
London, SW7 2AZ, UK

The spreading, imbibition and solidification of a hot two-dimensional droplet on a cooler porous substrate is studied. Lubrication theory and asymptotic reduction are used to derive a coupled system of evolution equations for the droplet thickness and vertical extents of the solid/melt boundary and the saturation front within the porous medium. This medium is assumed to be a membrane composed of an array of pores having fixed width. A precursor layer model and a disjoining pressure are used to relieve the singularity at the contact line. When the solidification and imbibition time scales are similar to those associated with spreading, the dynamics follow two stages: spreading and imbibition accompanied by solidification within the pores leading to their blockage, followed by contact line arrest and basal solidification of the droplet; the possibility of crust formation at the gas–melt interface is excluded from the present study. The dependence of the dynamics on the relevant system parameters is elucidated. Furthermore, our modelling predictions compare favourably with experimental data also obtained as part of the present work.

---

1. Introduction

The dynamics of droplet spreading on the surface of solid substrates is central to numerous applications and has therefore received considerable attention in the literature over the past four decades (see the review by Oron, Davis & Bankoff 1997 and references therein). On relatively high-energy surfaces, a liquid droplet is driven to spread by capillarity and gravity over ultra-thin precursor layers, which form rapidly ahead of the droplet. On relatively low-energy surfaces, on the other hand, a droplet assumes a static shape, characterized by a finite contact angle. In the case of dynamic spreading, the apparent or macroscopic contact angle is dependent on the flow characteristics, the properties of the liquid and the underlying solid. At the contact line, the no-slip condition implies that infinite stress is required in order to bring about droplet spreading; this is the so-called contact line 'singularity', which has been the subject of many studies (Oron *et al.* 1997).

Although droplet spreading over impermeable substrates has been much studied, that over permeable solids has received less attention. This is surprising since this problem is of interest for systems involving spreading over textiles, spray-painting, inkjet-printing on paper, particle agglomeration and spreading of gravity currents over

---

† Author to whom correspondence should be addressed: o.matar@imperial.ac.uk

porous solids (Washburn 1921; Davis & Hocking (1999, 2000); Aradian, Raphael & de Gennes 2000; Acton, Huppert & Worster 2001; Clarke *et al.* 2002; Holman 2002; Starov *et al.* 2002*a–c*; Alleborn & Raszillier 2004; Warren 2004). Denesuk *et al.* (1993) studied the dewetting and capillary-driven penetration of small droplets into porous substrates consisting of an array of parallel cylinders of constant radius using the Washburn equation. Work related to paper coating was also carried out using simple models for liquid penetration into the porous medium (Sunderhauf, Raszillier & Durst 1999). Davis & Hocking (1999, 2000) used lubrication theory to examine the spreading of two-dimensional droplets over porous media composed of arrays of vertical pores of constant width and finite length. Their asymptotic and brief numerical investigations yielded valuable information regarding the behaviour near the contact line, the time scales of the dynamics in various situations and their dependence on system parameters. Clarke *et al.* (2002) and Starov (2002*a–c*) also studied the spreading and imbibition problem in connection with coating and ink-jet printing, while Holman *et al.* (2002) considered this system in connection with fabrication of ceramic components on a micrometre-scale using ink-jet printing technology. Clarke *et al.* (2002) and Holman *et al.* (2002) both observe that the droplet rapidly assumes a spherical cap shape under the action of capillarity following its release and subsequent impact on the substrate. In order to evolve the location of the contact line, Holman *et al.* (2002) used an empirical power-law model, akin to Tanner's law (Tanner 1979) while Clarke *et al.* (2002) related the radial rate of advance of the contact line to the dynamic contact angle using molecular-kinetic theory; imbibition into the porous medium was modelled using the Washburn equation. Alleborn & Raszillier (2004) used lubrication theory to study the spreading of axisymmetric droplets on porous substrates by adopting a precursor layer model; Darcy's law is used to model the imbibition process, which is characterized by a front separating the saturated from the unsaturated regions of the porous medium. These authors also examine complicated three-dimensional spreading and imbibition situations.

The studies reviewed thus far have all involved isothermal spreading. Interesting situations arise, however, in cases where the spreading of solidifying melts occurs and non-isothermal effects and phase-changes take place. Flows involving phase changes are complicated by the presence of an additional free surface, which represents the boundary between the solidified and melt phases. These systems are of interest in a variety of situations involving geophysical flows, for instance, such as gravity currents and lava flows (Bercovici & Lin 1996; Simpson 1997; Balmforth & Craster 2000; Griffiths 2000; Balmforth, Craster & Sassi 2004), ice sheets and accretion (Baral, Hutter & Greve 2001; Myers, Charpin & Chapman 2002), the cooling of core melts inside a nuclear reactor (Bunk 1999) and crystallization as well as agglomeration (see Anderson, Worster & Davis 1996 and references therein). Several studies have attempted to model the dynamics of non-isothermal spreading in the absence of solidification but with substantial changes in the viscosity (Sakimoto & Zuber 1995; Bercovici & Lin 1996; Balmforth & Craster 2000; King, Riley & Sansom 2000), and with solidification (Bunk 1999; Bunk & King 2003). To the authors' best knowledge, however, no studies are available that have examined droplet spreading and imbibition on a porous medium with solidification. This problem represents the focus of this work.

The problem treated in this paper has been motivated by the industrial process of coating, which, among other applications, is the final step in the manufacture of most pharmaceutical tablets intended for oral administration. Tablets are coated for several reasons: for taste masking in order to isolate the often unpleasant taste of active pharmaceutical ingredients (APIs), for mechanical protection to prevent tablet

attrition and edge chipping during manipulation and transport, and finally to reduce atmospheric moisture absorption by hygroscopic ingredients that may be present in the tablet (Teunou & Poncelet 2002). The coating process involves the spraying of fine droplets of a polymer melt or solution onto the surface of the tablets. In order to create a coating layer on the surface rather than saturate the internal pore space of the tablet, the droplets must solidify before being completely drawn by capillary forces into the tablet. On the other hand, the solidification must not be too fast, otherwise the coating layer would be rough and too much material would have to be used for a complete coverage of the tablet surface. It is therefore important to understand the effect of three simultaneously occurring physical phenomena: droplet spreading, imbibition, and solidification, on the dynamics of the coating process and the resulting morphology of the solidified droplet.

In the present paper, we investigate the spreading and imbibition dynamics of hot two-dimensional droplets on a cooler porous medium, whose temperature is lower than the melting point of the droplet. This, then, leads to solidification of the melt within the pores ultimately leading to their blockage, and brings about the end of the spreading and penetration stage of the dynamics. In the second stage, the droplet undergoes basal solidification. Lubrication theory is used to derive a model consisting of three evolution equations for the droplet thickness, penetration depth as well as the height of the solid/melt front; the latter was obtained following the solution of the temperature field within the solid and fluid phases in the drop. These equations are parameterized by appropriate dimensionless groups reflecting the relative importance of the relevant hydrodynamic and heat transfer mechanisms. Note that we shall follow the work of Schwartz & Eley (1998) and Alleborn & Raszillier (2004) and relieve the contact line singularity at the edge of the drop by using a precursor layer and a disjoining pressure model. Experimental studies are also conducted in order to validate the predictions of the model. A parametric study is presented in which the dependence of the dynamics on the relevant parameters is elucidated and numerical solutions are also compared with experimental data yielding favourable agreement.

The rest of this paper is organized as follows. In §2, we present our experimental results, while in §3, a presentation of the problem formulation is provided, which contains details of the different scalings adopted within the medium and drop regions and of the derivation of the evolution equations. Section 4 is dedicated to the discussion of the numerical results and in §5 we provide comparisons between theory and experiment and discuss model limitations. Finally, concluding remarks are provided in §6.

2. Experimental

In this section, we present the results of our experimental investigation of the spreading, imbibition and solidification of droplets on porous media. We begin by describing the experimental set-up and procedure used to carry out the study. The experimental results are then discussed.

2.1. *Materials and methods*

The spreading, penetration and solidification dynamics of polyethylene glycol (PEG) melts on porous tablets made of anhydrous sodium carbonate were studied experimentally. These materials have been selected for the following reasons: sodium carbonate is a typical example of a filler material used in tablet formulations, and PEGs are edible water-soluble polymers often used as binders in tableting and granulation, providing a range of melting points and melt viscosities, depending on
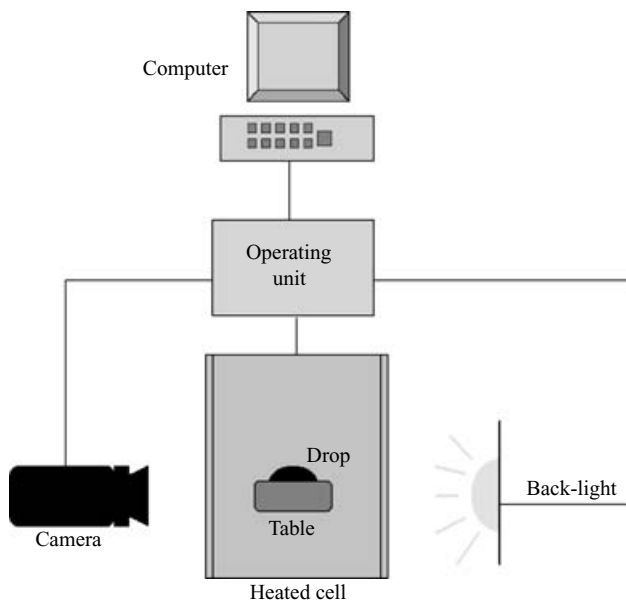
FIGURE 1. Schematic representation of the apparatus used for the experimental measurement
of the droplet spreading dynamics.

the chosen PEG molecular weight. (Note that although PEGs exhibit slight differences between their melting and solidification points owing to hysteresis, these differences will be considered negligible below.) Tablets were compressed at 3 Mt in a 13 mm die from particle size fraction of 125–150 μm which was obtained by sieving. The mass of all tablets was kept constant at 1.0 g. In order to realize systems with different viscosity, polyethylene glycols of two different molecular weights – PEG1500 and PEG4000 – have been used. Their melting points and melt viscosities are $T_m = 45\,^\circ$C and $\mu = 0.188$ Pa s for PEG1500, and $T_m = 62\,^\circ$C, and $\mu = 0.415$ Pa s for PEG4000, respectively.

A commercially available instrument DSA-10 (Kruss GmbH) was used for recording the droplet spreading dynamics; a schematic drawing of the instrument set-up is shown in figure 1. The substrate (tablet) was placed onto a controlled-temperature stage and a droplet of PEG melt was deposited on the tablet from a heated syringe. The profile of the spreading droplet was recorded at a high frame rate (typically 60 f.p.s.) by a digital camera connected to a PC with a frame-grabber card. The temporal evolution of the droplet base diameter, height and dynamic contact angle were obtained by automatic image analysis of the recorded spreading sequences. The 'spherical cap' method was found to be the most appropriate for approximating the droplet shape. The final distribution of solidified PEG within the tablet was also analysed. The tablets were carefully fractured in such a way that the fracture bisects the droplet. In order to increase contrast between the penetrated PEG and the original tablet material, the fractured face was coloured using a water-based ink, which preferentially coloured the sodium carbonate substrate. A digital image of the fractured tablet was then recorded.

2.2. Discussion of results

Droplet spreading sequences and the final distribution of solidified PEG1500 in the tablet are shown in figures 2, 3 and 4 for three qualitatively different situations
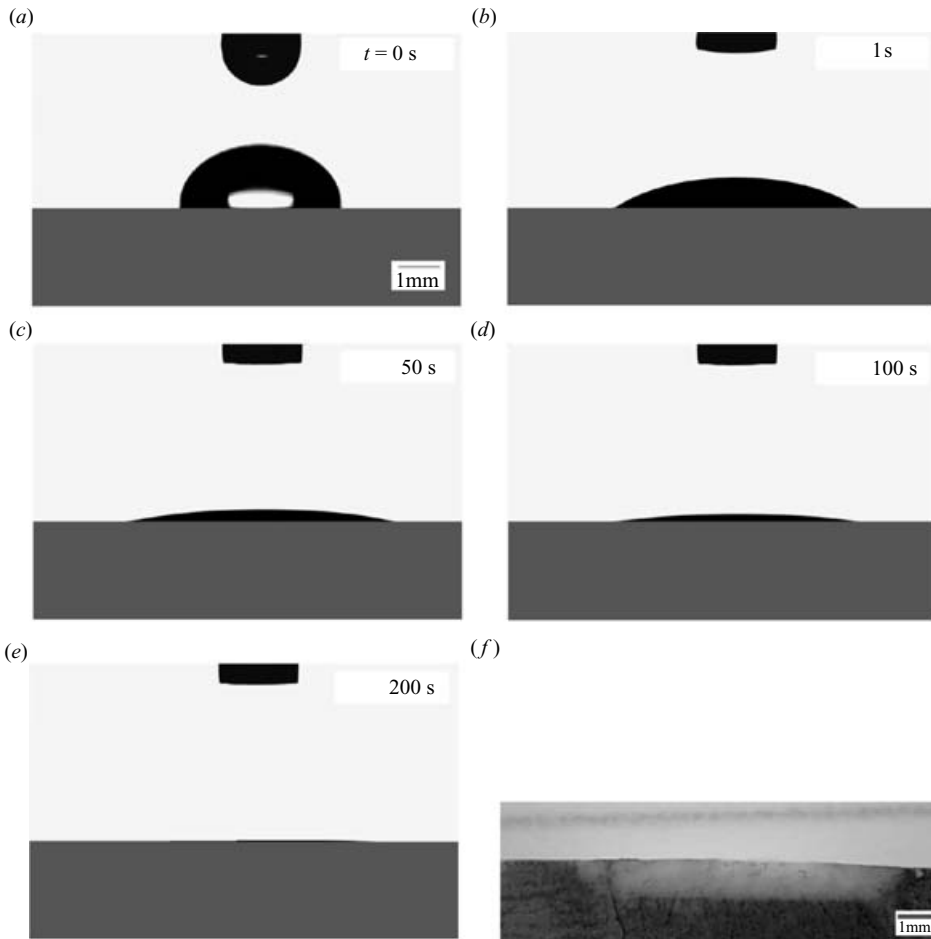
FIGURE 2. Evolution of droplet shape for PEG1500 melt on a sodium carbonate tablet when no solidification occurs during spreading (*a–e*); the substrate and droplet temperatures are 45.5°C and 47°C, respectively. (*f*) An image of the fractured substrate revealing the final distribution of PEG within the tablet.

representing the cases of no solidification during spreading (figure 2), simultaneous solidification and spreading (figure 3), and almost instantaneous solidification in pores (figure 4). The substrate was given an artificial colour in the figures in order to make it easier to distinguish the droplet profile from the baseline during the latter stages of the spreading (in the original images the substrate was black).

The no-solidification case (figure 2) was realized by heating the tablet above the melting point of PEG1500. The sequence shows the phenomenon of spreading to a maximum diameter and then retraction of the contact line owing to continuing penetration of the droplet into the substrate. The maximum base diameter is given by the diameter of the penetrated PEG apparent in figure 2(*f*). In the intermediate case (figure 3), the diameter of the residual solidified droplet is less than the maximum base diameter, and there is a characteristic plateau of constant penetration depth, which is due to solidification-induced pore-blocking. The rapid solidification case (figure 4) was realized by maintaining the tablet below the melting point of PEG1500. Nevertheless, some penetration still occurred owing to local heating-up of the substrate by the
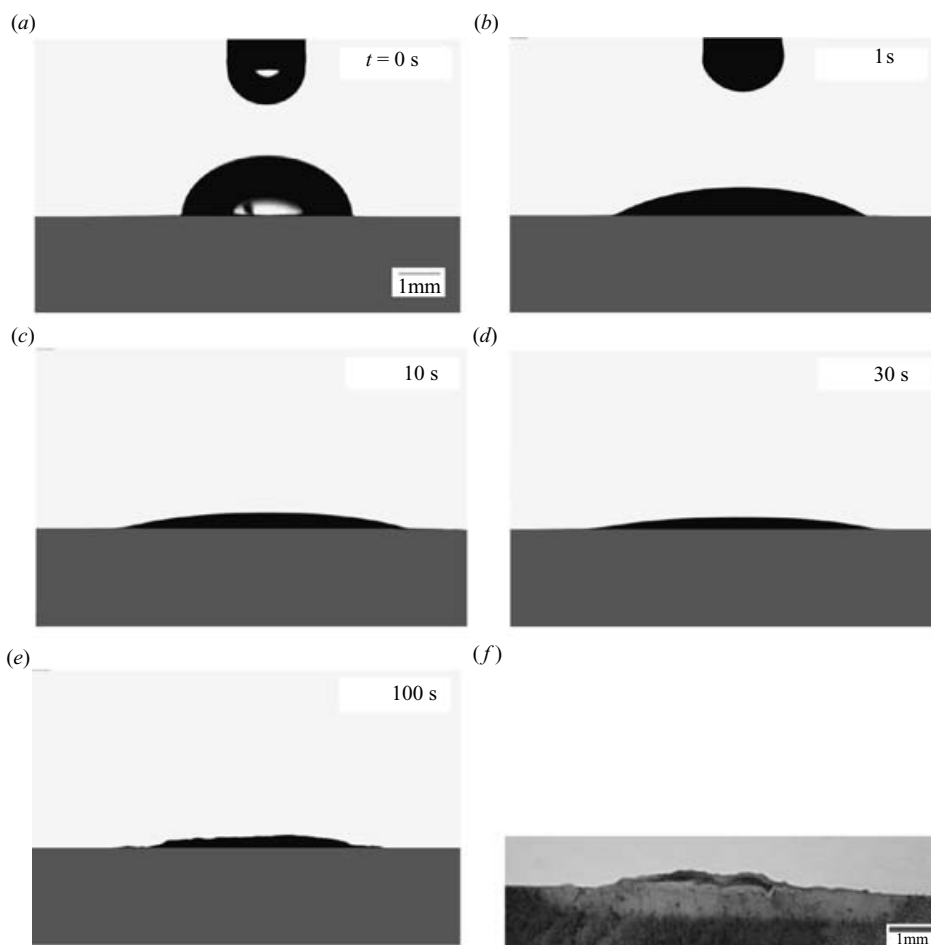
FIGURE 3. Evolution of droplet shape for PEG1500 melt on a sodium carbonate tablet in the case of simultaneous solidification and spreading (*a–e*); the substrate and droplet temperatures are 40 °C and 47 °C, respectively. (*f*) An image of the fractured substrate revealing the final distribution of PEG within the tablet.

drop, as can be seen in figure 4(*f*). The level of penetration in this case, however, was substantially lower than that achieved in the cases of no-solidification and simultaneous solidification and penetration (see figures 2*f* and 3*f*).

We have also investigated experimentally the effect of system parameters on the spreading dynamics. The dependence of the droplet base diameter and the dynamic contact angle on time for PEG1500 and several combinations of substrate and droplet temperatures are plotted in figure 5. To make individual experiments comparable, the base diameter is shown in a dimensionless form, i.e. it is always scaled by the initial base diameter. Curves 1 and 2 in figure 5 correspond to the rapid solidification situation: the contact line is frozen at a certain maximum base diameter, which is somewhat lower for colder substrates (curve 1). Also, the apparent contact angle of the frozen droplet is larger when solidification is faster (curve 1). Curve 3 represents a case with partial solidification, while curves 4 and 5 are for no solidification (the substrate temperature is above the melting point.) The fact that the maximum base diameter is highest in case 5 can be explained by its lowest viscosity. We can also
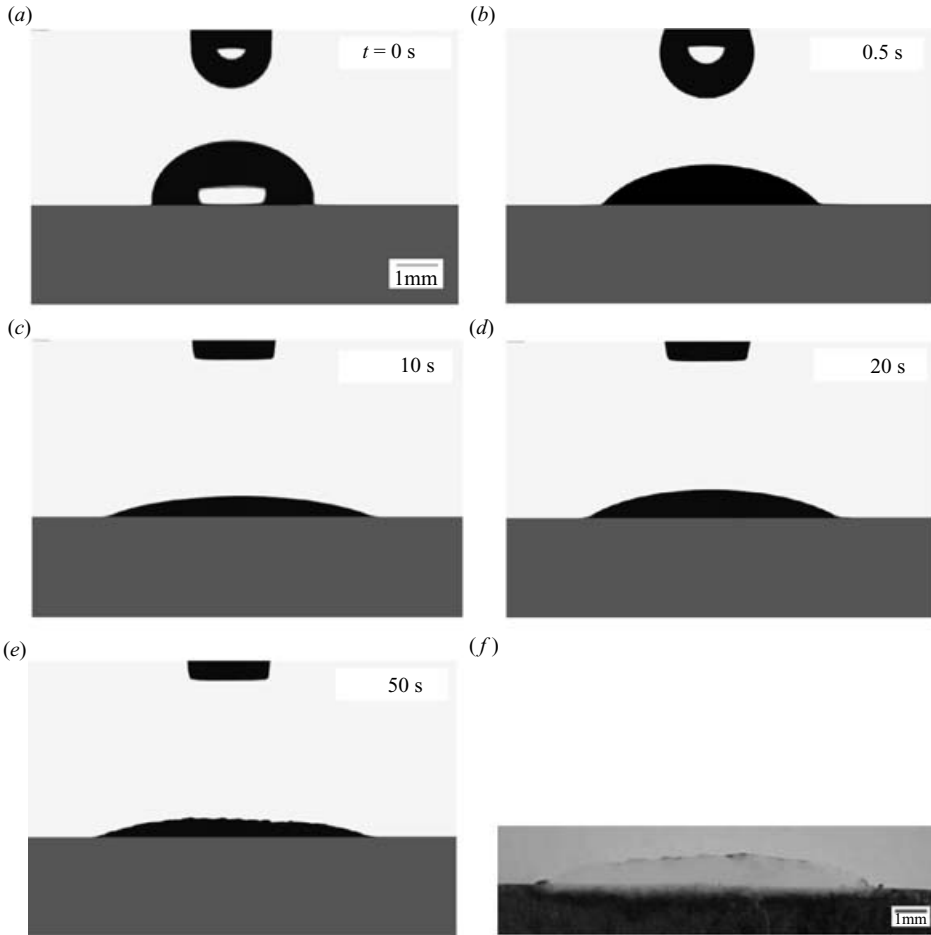
FIGURE 4. Evolution of droplet shape for PEG1500 melt on a sodium carbonate tablet in the limiting case of fast solidification (*a–e*); the substrate and droplet temperatures are 30°C and 47°C, respectively. (*f*) An image of the fractured substrate revealing the final distribution of PEG within the tablet.

see that the degree to which the contact line retracted is lowest in that case because the droplet has completely penetrated into the substrate faster than in cases 3 and 4, presumably owing to the lower viscosity in case 5.

A comparison between the droplet spreading and solidification dynamics for PEG1500 and PEG4000 for several combinations of substrate and droplet temperatures is shown in figure 6. Curve 1 is the rapid solidification case for PEG1500 which has already been discussed; attention will therefore be focused on the curves labelled '2'–'5' in figure 6(*a*). The curves labelled '2' in figure 6 demonstrate the absence of solidification since $T_s > T_m$ in this case; moreover, the spreading rate appears to be faster than in case 1 owing to the decreased viscosity in 2 (since $T_d = 50°C$ and 60°C in cases 1 and 2, respectively). For the same reasons, the spreading rate in case 3 exceeds that in cases 1 and 2. Curves 4 and 5, which are for the higher-viscosity PEG4000, clearly show slower spreading dynamics during the initial stages of the spreading process. The substrate temperature in case 4, $T_s = 60°C$, is slightly below the melting point of PEG4000, $T_m = 62°C$, which indicates that solidification is
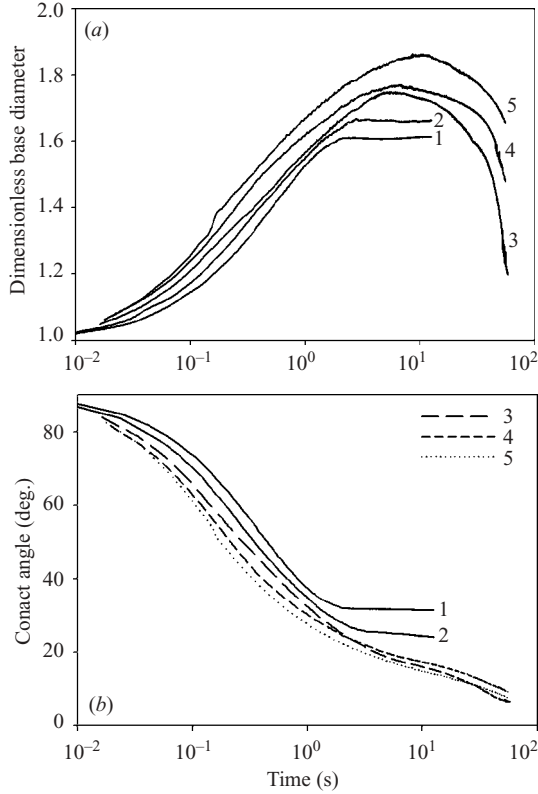
FIGURE 5. The effect of temperature on PEG1500 droplet spreading and solidification dynamics: (*a*) droplet base diameter, (*b*) dynamic contact angle. The substrate and initial droplet temperatures are: curve 1: $T_s = 30\,^\circ$C, $T_d = 50\,^\circ$C; curve 2: $T_s = 40\,^\circ$C, $T_d = 50\,^\circ$C; curve 3: $T_s = 40\,^\circ$C, $T_d = 60\,^\circ$C; curve 4: $T_s = 50\,^\circ$C, $T_d = 60\,^\circ$C; curve 5: $T_s = 50\,^\circ$C, $T_d = 70\,^\circ$C.

indeed possible in this case. In case 5, $T_s > T_m$, thus no solidification will occur, but T_d is lower than that in case 4 which implies that the viscosity in this case is larger. However, the highest maximum base diameter is attained by PEG4000 (curve 5), which may be due to the slower penetration rate, and therefore larger liquid volume available for spreading. This hypothesis is also supported by the fact that the contact line retraction rate (the slope of the base diameter *vs.* time curves in the final phase) is much slower for PEG4000 (curves 4 and 5) than for the lower viscosity PEG1500.

The case of PEG considered so far represents a system where the density of the solid and melt are practically equal (that is, there is no change in volume upon solidification). In order to realize a situation where a substantial change in volume does occur, the solidification of water droplets on a cold impermeable substrate was studied. A sequence of droplet shape evolution profiles for a water droplet of initial temperature $T_d = 25\,^\circ$C on an impermeable substrate of temperature $T_s = -20\,^\circ$C is shown in figure 7. This case is characterized by large Stefan numbers due to the relatively small magnitude of the viscosity of water. Close inspection of figure 7 reveals that the formation of a cusp-like feature near the apex of the solidifying droplet becomes apparent at the latter stages of the dynamics (figure 7*e*, *f*). This is very similar to the shapes of solidified droplets in the work of Anderson *et al.*
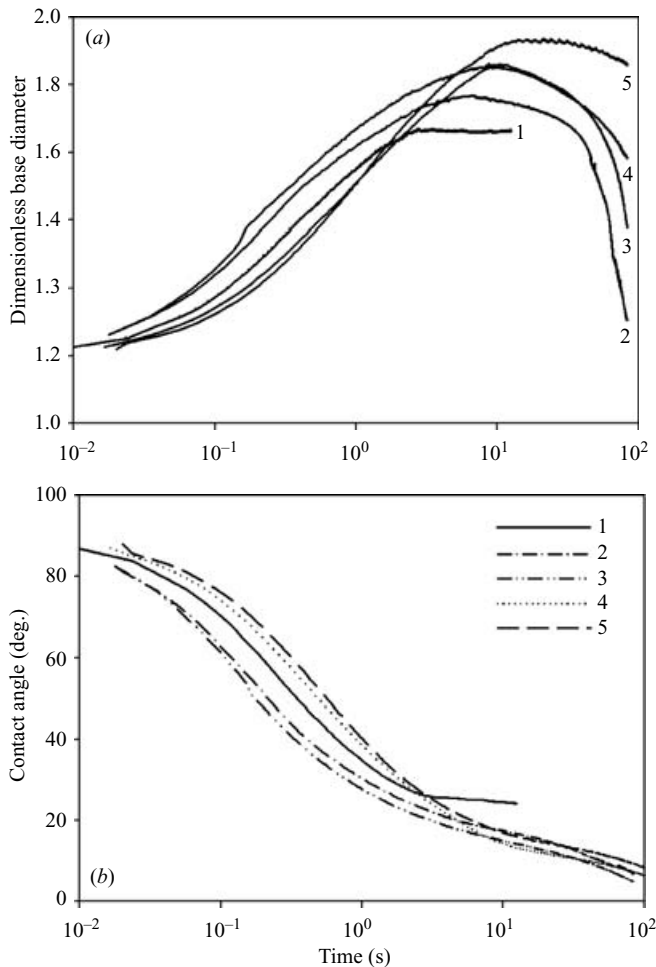
FIGURE 6. The effect of viscosity and temperature on droplet spreading and solidification dynamics: (*a*) droplet base diameter, (*b*) dynamic contact angle. The conditions are: curve 1: $T_s = 40\,°C$, $T_d = 50\,°C$, PEG1500; curve 2: $T_s = 50\,°C$, $T_d = 60\,°C$, PEG1500; curve 3: $T_s = 50\,°C$, $T_d = 70\,°C$, PEG1500; curve 4: $T_s = 60\,°C$, $T_d = 80\,°C$, PEG4000; curve 5: $T_s = 70\,°C$, $T_d = 65\,°C$, PEG4000.

(1996) and will be compared to our modelling predictions in §5 below. The model formulation is presented next.

3. Problem formulation

3.1. *Preliminary considerations*

We consider the spreading dynamics of a drop of Newtonian and incompressible fluid, of viscosity μ, density ρ, thermal conductivity λ, and specific heat capacity C_p, on a porous medium. The drop has characteristic height and length scales h_0 and a_0, respectively; the aspect ratio of the drop, $\epsilon \equiv h_0/a_0$, will be taken to be sufficiently small so as to permit the use of lubrication theory. The dynamics of the essentially inviscid gas overlying the drop will be neglected. The drop profile subtends an apparent contact angle, θ_a, with the underlying porous medium. The
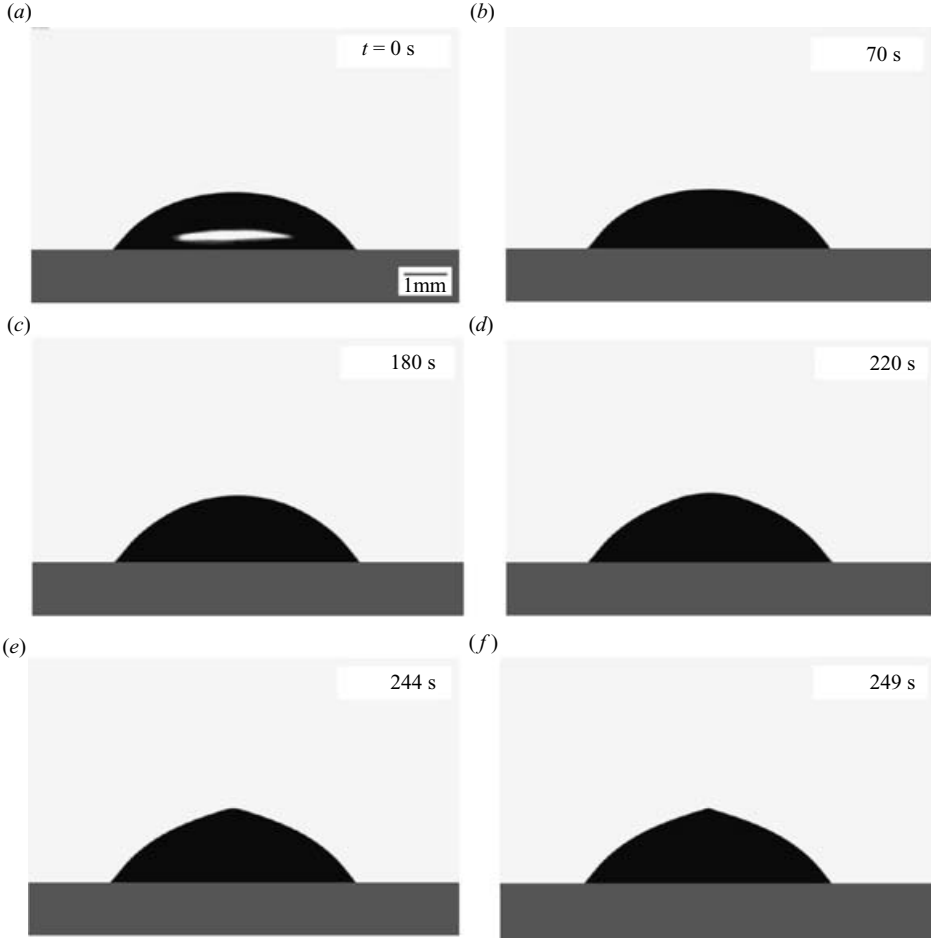
FIGURE 7. Shape evolution of a freezing water droplet on a cold, impermeable substrate. Here, the substrate and initial droplet temperatures are $-20\,^{\circ}$C and $25\,^{\circ}$C, respectively.

drop will therefore spread or dewet depending on whether θ_a is larger or smaller than θ_e, the equilibrium contact angle. In the present work, θ_e is obtained via use of a model proposed by Schwartz & Eley (1998), which involves an appropriately defined disjoining pressure, Π, and a precursor layer thickness, h_*.

The porous medium is taken to be partially saturated with the same fluid as that which constitutes the drop. The saturated and unsaturated regions in the medium are separated by a front, which is assumed to be sharp. The medium is composed of vertical pores of width $2b$ with a number density n per unit width. As the drop spreads over the porous medium, fluid from the drop will penetrate through the pores. The temperature of the medium, T_w, which is assumed to be constant, is sufficiently lower than the melting point of the spreading fluid, T_m. Thus the spreading process is accompanied by solidification within the pores, resulting, ultimately, in their blockage. This, then, demarcates the end of the first stage of the spreading dynamics. Owing to the solidification process, the permeability, K, and porosity, ϕ, of the medium are both expected to be time-dependent. Closed-form expressions for K, ϕ, and the average velocity within the medium, W, will be determined by examining the flow
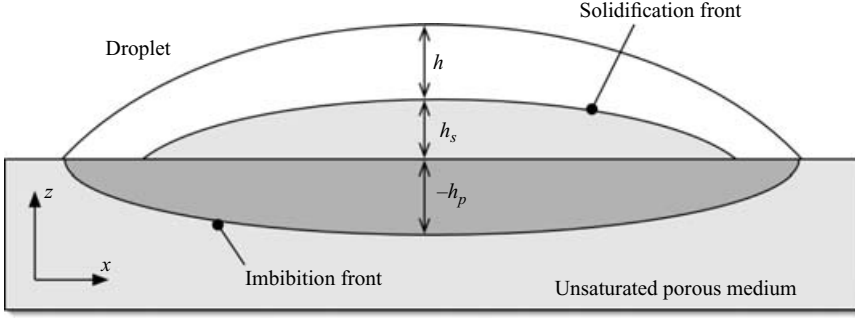
FIGURE 8. The flow geometry.

and accompanying heat transfer therein. These expressions will provide an input into the equations governing the dynamics of the spreading process.

The second stage involves the continued spreading of the drop accompanied by the development of an underlying layer of its own solid phase; the bottom surface of this layer coincides with the top surface of the porous medium. This stage involves the close approach of the solid–liquid and air–liquid interfaces, which will promote the liquid to dewet its own solid phase. As mentioned above, this will occur if the apparent dynamic contact angle is smaller than the equilibrium contact angle. This will arise naturally owing to the inclusion of a disjoining pressure, Π, in the momentum conservation equations, which includes both attractive and repulsive intermolecular interactions.

Because of the disparity of scales, which exists naturally within this problem, a multi-scale approach is adopted. The scalings, which will be adopted in the porous medium will be different from those used in the drop. We begin, however, by presenting the equations governing the flow in both the drop and porous medium.

3.2. *Governing equations: the drop*

We use a rectangular coordinate system to describe the dynamics. The velocity field in the drop is expressed by $\boldsymbol{u} = (u, 0, w)$, in which u and w correspond to the velocity components in the horizontal and vertical directions, x and z, respectively. As shown in figure 8, the top surface of the porous medium and the air–liquid interface are located at $z = 0$ and $z = h(x, t) + h_s(x, t)$, respectively, while the sharp front separating the saturated and the unsaturated regions of the porous medium is located at $z = -h_p(x, t)$. Here, the interface between the liquid and solid phases in the drop, where the temperature is $T = T_m$, is located at $z = h_s(x, t)$. Note that this interface is assumed to be sharp and the possibility of formation of a 'mushy zone', which can arise in situations involving ice-sheets (Greve 1997), for instance, is not considered in the present work.

The equations governing the flow within the drop are therefore given by

$$u_x + w_z = 0, \tag{3.1}$$
$$(p - \Pi)_x = \mu u_{zz}, \tag{3.2}$$
$$p_z = -\rho g, \tag{3.3}$$

which correspond to continuity and the x and z components of the Navier–Stokes equations, respectively, where the subscript denotes partial differentiation unless stated otherwise. Here, p and g denote the pressure in the fluid and the acceleration due to

gravity, respectively. The disjoining pressure is given by

$$\Pi = \frac{A}{h_*^n}\left[\left(\frac{h_*}{h}\right)^n - \left(\frac{h_*}{h+h_s}\right)^n - \left(\left[\frac{h_*}{h}\right]^m - \left[\frac{h_*}{h+h_s}\right]^m\right)\right],\qquad(3.4)$$

where the coefficient A is related to n, m and the equilibrium contact angle, θ_e, through $A = \sigma\theta_e^2(n-1)(m-1)/2(n-m)h_*$ assuming small θ_e; here, $(n,m) = (2,3)$.

These equations are complemented by boundary conditions, which are time-dependent:

$$u = 0 \quad \text{at } z = h_s,\qquad(3.5)$$

which is the no-slip condition, while continuity of the normal component of the velocity is

$$w = WH(t_1 - t) + [1 - H(t_1 - t)](1 - \mathscr{R})h_{st} \quad \text{at } z = h_s,\qquad(3.6)$$

where $H(t_1 - t)$ is the Heaviside function. Here, W is the average speed of the flow in the porous medium, which will be obtained via solution of the flow equations in this medium and invoking Darcy's law; t_1 denotes the duration of the first stage of the spreading process beyond which $W = 0$ owing to pore blockage. The condition on w for $t > t_1$ was obtained by demanding continuity of mass flux at h_s in the lubrication approximation, where $\mathscr{R} \equiv \rho_s/\rho$, a ratio of the solid to melt densities. Note that the thickness of the solidified layer is

$$h_s = 0 \quad \text{for} \quad t \leqslant t_1.\qquad(3.7)$$

The other boundary conditions correspond to continuity of the shear and normal stress components at $z = (h + h_s)(x,t)$ and the kinematic boundary condition at this interface; these, in the lubrication approximation, are respectively given by

$$u_z = 0,\qquad(3.8)$$
$$p = -\sigma(h + h_s)_{xx},\qquad(3.9)$$
$$h_t + uh_x = w,\qquad(3.10)$$

where σ denotes the surface tension of the air–liquid interface. Here, we have implicitly assumed the absence of thermally induced Marangoni stresses. Equation (3.10) may be re-expressed by

$$h_t + Q_x = WH(t_1 - t) - [1 - H(t_1 - t)]\,\mathscr{R}h_{st},\qquad(3.11)$$

where $Q = \int_{h_s}^{h} u\,\mathrm{d}z$ is the volumetric flow rate. Additionally, we demand continuity of pressure at $z = 0$ for $t \leqslant t_1$.

The energy conservation equation for the fluid phase is given by

$$\rho C_p\,(T_t + uT_x + wT_z) = \lambda\,(T_{xx} + T_{zz}),\qquad(3.12)$$

where T denotes temperature; note that we have implicitly assumed that viscous heat generation is negligible. A similar energy conservation equation is used for the solidified phase, in which the same quantities arise but are decorated with a distinguishing 's' subscript:

$$\rho_s C_{p_s} T_{st} = \lambda_s\,(T_{s_{xx}} + T_{s_{zz}});\qquad(3.13)$$

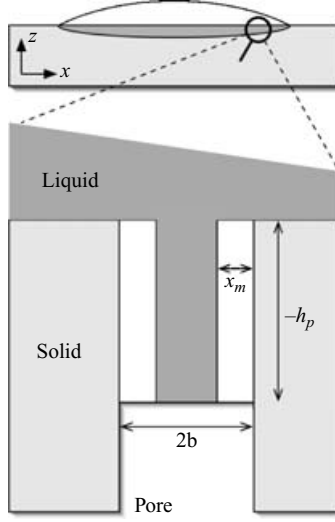here, 's' denotes quantities in the solid phase.

FIGURE 9. The adopted geometry for the porous medium.

Equation (3.12) is solved subject to the following boundary conditions in the lubrication approximation

$$-\lambda T_z = \alpha \left(T - T_a \right) \quad \text{at } z = h + h_s, \tag{3.14}$$

$$T = T_w H(t_1 - t) + [1 - H(t_1 - t)] T_m \quad \text{at } z = h_s. \tag{3.15}$$

Equation (3.14) corresponds to a flux condition at the interface in which T_a denotes the temperature of the surroundings and α is a heat transfer coefficient. Solutions of (3.13) are obtained subject to

$$T_s = T_m \quad \text{at } z = h_s, \tag{3.16}$$

and continuity of temperature at the base, assumed to be perfectly conducting:

$$T_s = T_w \quad \text{at } z = 0. \tag{3.17}$$

We have also performed an energy balance at $z = h_s$, which, in the lubrication approximation, yields

$$h_{st} = \frac{\lambda_s}{\rho_s \Delta H_m} \left(T_{s_z} - \mathcal{L} T_z \right), \tag{3.18}$$

where continuity of mass flux at $z = h_s$ was also used and $\mathcal{L} \equiv \lambda / \lambda_s$. This balance reflects the fact that the latent heat of fusion, ΔH_m, released during the solidification process, is conducted away from $z = h_s$ in the solidified and molten phases. Thus, specification of the temperature field in both phases yields an evolution equation for h_s. We turn now to the equations in the porous medium.

3.3. Governing equations: porous medium

We assume that the pores in the porous medium are long and thin (see figure 9) so that the flow is governed by the following equations

$$\hat{u}_{\hat{x}} + \hat{w}_{\hat{z}} = 0, \tag{3.19}$$

$$\hat{p}_{\hat{z}} = -\rho g + \mu \hat{w}_{\hat{x}\hat{x}}, \tag{3.20}$$

$$\hat{p}_{\hat{x}} = 0, \tag{3.21}$$

where $\hat{u}$, $\hat{w}$ and $\hat{p}$ denote the horizontal and vertical components of the velocity field, and the pressure within the pores, respectively. The flow through these pores over the region $0 \geqslant \hat{z} \geqslant -h_p$ is taken to be of the Poiseuille type driven by a pressure gradient equal to $\left[\hat{p}(\hat{z} = 0) - \hat{p}(\hat{z} = -h_p)\right] / h_p$, where $\hat{p}(\hat{z} = -h_p)$ is a capillary pore pressure, given by

$$\hat{p}(\hat{z} = -h_p) = -\frac{2\sigma}{(b - \hat{x}_m)}, \tag{3.22}$$

where $\hat{x} = \hat{x}_m(t)$ denotes the interface between the solidified and fluid phases within the porous medium.

Equation (3.20) is solved subject to the following symmetry and no-slip conditions, respectively, given by

$$\hat{w}_{\hat{x}} = 0 \quad \text{at } \hat{x} = b, \tag{3.23}$$
$$\hat{w} = 0 \quad \text{at } \hat{x} = \hat{x}_m(t). \tag{3.24}$$

Note that the no-slip condition was applied at $\hat{x} = \hat{x}_m(t)$. Also, continuity of mass flux at $\hat{x} = \hat{x}_m(t)$ yields

$$\hat{u} = (1 - \mathscr{R})\dot{\hat{x}}_m. \tag{3.25}$$

The energy conservation equation for the fluid phase in the porous medium is given by

$$\rho C_p(\hat{T}_{\hat{t}} + \hat{u}\hat{T}_{\hat{x}} + \hat{w}\hat{T}_{\hat{z}}) = \lambda(\hat{T}_{\hat{x}\hat{x}} + \hat{T}_{\hat{z}\hat{z}}), \tag{3.26}$$

while that for the solidified phase in the region $0 \leqslant \hat{x} \leqslant \hat{x}_m$ is similar except for the distinguishing 's' subscript:

$$\rho_s C_{p_s}\hat{T}_{s_{\hat{t}}} = \lambda_s(\hat{T}_{s_{\hat{x}\hat{x}}} + \hat{T}_{s_{\hat{z}\hat{z}}}). \tag{3.27}$$

In (3.26) and (3.27), $\hat{T}$ and $\hat{T}_s$ denote the temperatures in the fluid and solidified phases, respectively, in the porous medium.

Equation (3.26) is solved subject to

$$\hat{T}_x = 0 \quad \text{at } \hat{x} = b, \tag{3.28}$$
$$\hat{T} = T_m \quad \text{at } \hat{x} = \hat{x}_m. \tag{3.29}$$

The temperature of the solidified phase, $\hat{T}_s$, satisfies the following boundary conditions

$$\hat{T}_s = T_w \quad \text{at } \hat{x} = 0, \tag{3.30}$$
$$\hat{T}_s = T_m \quad \text{at } \hat{x} = \hat{x}_m. \tag{3.31}$$

An energy balance at $\hat{x} = \hat{x}_m(t)$ is also performed which yields

$$\dot{\hat{x}}_m = \frac{\lambda_s}{\rho_s \Delta H_m}\left(\hat{T}_{s_x} - \mathscr{L}\hat{T}_x\right), \tag{3.32}$$

where we have also used (3.25). Knowledge of $\hat{T}$ and $\hat{T}_s$ allows the explicit determination of $\hat{x}_m(t)$. Finally, the dynamics of the front h_p are governed by

$$\phi h_{p_t} = -W, \tag{3.33}$$

where ϕ is the porosity of the porous medium.

3.4. *Scaling*

The governing equations and boundary conditions within the drop are rendered dimensionless by using the following scalings:

$$x = a_0 \tilde{x}, \quad (z, h, h_s) = h_0(\tilde{z}, \tilde{h}, \tilde{h}_s), \quad (u, w) = \mathscr{U}(\tilde{u}, \epsilon \tilde{w}),$$

$$(p, \Pi) = \mathscr{P}(\tilde{p}, \tilde{\Pi}), \quad t = (a_0/\mathscr{U})\tilde{t}, \quad T = T_w + (T_m - T_w)\tilde{T}, \tag{3.34}$$

in which $\mathscr{P}$ and $\mathscr{U}$ correspond to the characteristic pressure and velocity scalings in the drop, respectively:

$$\mathscr{P} \equiv \frac{\sigma h_0}{a_0^2}, \quad \mathscr{U} \equiv \frac{\sigma h_0^3}{\mu a_0^3}. \tag{3.35}$$

Here, the quantities with a tilde are dimensionless. Substitution of these scalings into the governing equations yields (after suppression of the tilde)

$$(p - \Pi)_x = u_{zz}, \tag{3.36}$$

$$p_z = -\mathscr{B}, \tag{3.37}$$

$$p = -(h + h_s)_{xx} \quad \text{at } z = h + h_s, \tag{3.38}$$

$$\epsilon Pe(T_t + uT_x + wT_z) = T_{zz} + O(\epsilon^2), \tag{3.39}$$

$$\epsilon Pe_s T_{st} = T_{szz} + O(\epsilon^2), \tag{3.40}$$

$$T_z = -B_s(T - \Theta_a) \quad \text{at } z = h + h_s, \tag{3.41}$$

$$T = 1 - H(t_1 - t) \quad \text{at } z = h_s, \tag{3.42}$$

$$T_s = 1 \quad \text{at } z = h_s, \tag{3.43}$$

$$T_s = 0 \quad \text{at } z = 0, \tag{3.44}$$

$$h_{st} = \frac{T_{sz} - \mathscr{L}T_z}{S} \quad \text{at } z = h_s. \tag{3.45}$$

Equations (3.1), (3.5)–(3.8) and (3.10) remain unaltered. The dimensionless disjoining pressure appearing in (3.36) is given by

$$\Pi = \mathscr{A}\left[\left(\frac{h_*}{h}\right)^n - \left(\frac{h_*}{h + h_s}\right)^n - \left(\left[\frac{h_*}{h}\right]^m - \left[\frac{h_*}{h + h_s}\right]^m\right)\right], \tag{3.46}$$

where $\mathscr{A} = a_0^2 A/(\sigma h_0) = 4/h_*$ (Schwartz & Eley 1998; Alleborn & Raszillier 2004) provides a dimensionless measure of the relative significance of disjoining pressure effects. In (3.36)–(3.42), the Bond number is given by $\mathscr{B} \equiv \rho g a_0^2/\sigma$ and the Péclet number in the fluid (solidified) phase is expressed by $Pe \equiv \rho C_p \mathscr{U} h_0/\lambda$ ($Pe_s \equiv \rho_s C_{p_s} \mathscr{U} h_0/\lambda_s$). The parameter $B_s \equiv \alpha h_0/\lambda$ is a surface Nusselt/Biot number while $S \equiv \rho_s \Delta H_m h_0^2 \mathscr{U}/(a_0 \lambda_s (T_m - T_w))$ is the Stefan number, which is a ratio between the time scales of energy release and conduction. Finally, $\Theta_a \equiv (T_a - T_w)/(T_m - T_w)$ is a dimensionless air temperature.

In the porous medium, the scalings adopted for space, time, the velocity field and pressure are different from those in the drop:

$$(\hat{x}, \hat{x}_m) = b\tilde{\hat{x}}, \quad \hat{z} = l\tilde{\hat{z}}, \quad (\hat{u}, \hat{w}) = \mathscr{W}(\hat{\epsilon}\tilde{\hat{u}}, \tilde{\hat{w}}), \quad \hat{p} = \left(\frac{\mu \mathscr{W} l}{b^2}\right)\tilde{\hat{p}}, \quad \hat{t} = \left(\frac{b}{\mathscr{U}}\right)\tilde{\hat{t}}, \tag{3.47}$$

where $\hat{\epsilon} \equiv b/l \ll 1$ is the aspect ratio of the pore in which l provides a measure of the pore length. The temperature scaling remains unaltered from (3.34) and the tilde decoration is dropped hereinafter. These scalings reflect the fact that the flow in the porous medium is driven by capillarity and resisted by viscous retardation.

The relevant dimensionless equations in the porous medium are then given by

$$\hat{p}_{\hat{z}} = -\hat{\mathscr{B}} + \hat{w}_{\hat{x}\hat{x}}, \tag{3.48}$$

$$\hat{w}_{\hat{x}} = 0 \quad \text{at } \hat{x} = 1, \tag{3.49}$$

$$\hat{w} = 0 \quad \text{at } \hat{x} = \delta, \tag{3.50}$$

$$\hat{\epsilon}\hat{P}e(\hat{T}_{\hat{t}} + \hat{u}\hat{T}_{\hat{x}} + \hat{w}\hat{T}_{\hat{z}}) = \hat{T}_{\hat{x}\hat{x}}, \tag{3.51}$$

$$\hat{\epsilon}\hat{P}e_s\hat{T}_{s_{\hat{t}}} = \hat{T}_{s_{\hat{x}\hat{x}}}, \tag{3.52}$$

$$\hat{T}_{\hat{x}} = 0 \quad \text{at } \hat{x} = 1, \tag{3.53}$$

$$\hat{T} = 1 \quad \text{at } \hat{x} = \delta, \tag{3.54}$$

$$\hat{T}_s = 1 \quad \text{at } \hat{x} = \delta, \tag{3.55}$$

$$\hat{T}_s = 0 \quad \text{at } \hat{x} = 0, \tag{3.56}$$

$$\dot{\delta} = \frac{\hat{T}_{s_x} - \mathscr{L}\hat{T}_x}{\hat{S}}, \tag{3.57}$$

$$\phi h_{p_{\hat{t}}} = -W. \tag{3.58}$$

Here, the Bond number in the porous medium is given by $\hat{\mathscr{B}} \equiv \rho g b l / \sigma$, $\delta = \hat{x}_m / b$ is the dimensionless location of the solidifying front, $\hat{P}e \equiv \rho C_p \mathscr{W} b / \lambda$ and $\hat{P}e_s \equiv \rho_s C_{p_s} \mathscr{W} b / \lambda_s$ are Péclet numbers in the fluid and solidifying phases, respectively, while the Stefan number in the porous medium is given by $\hat{S} \equiv \rho_s b^2 \mathscr{W} \Delta H_m / (\lambda_s (T_m - T_w) l)$.

3.5. *Evolution equations*

In this section, we derive the evolution equations which govern the dynamics of the drop at the different stages of the flow. Integration of (3.37) and application of (3.38) gives rise to the following pressure field

$$p = -(h + h_s)_{xx} + \mathscr{B}(h + h_s - z). \tag{3.59}$$

Since p_x is independent of z, integration of (3.36) and application of (3.5) and (3.8) yields

$$u = \tfrac{1}{2} p_x (z - h_s)[z - (h_s + 2h)]. \tag{3.60}$$

In the case, $(Pe, Pe_s) \ll 1$, (3.39) and (3.40) simply become

$$T_{zz} = 0, \qquad T_{s_{zz}} = 0. \tag{3.61}$$

Thus, integration of these equations and application of (3.41)–(3.44) yields the following temperature distributions in the fluid and solid phases within the drop:

$$T = 1 + \frac{B_s(\theta_a - 1)(z - b)}{1 + B_s h}, \tag{3.62}$$

$$T_s = \frac{z}{b}. \tag{3.63}$$

Substitution of (3.62) and (3.63) into (3.45) then gives a dimensionless evolution equation for h_s:

$$h_{st} = \frac{1}{S}\left[\frac{1}{h_s} - \frac{\mathscr{L}B_s(\Theta_a - 1)}{1 + B_s h}\right]. \tag{3.64}$$

In order to derive an evolution equation for h, W must be specified. Assuming that $(\hat{P}e, \hat{P}e_s) \ll 1$, then

$$\hat{T}_{\hat{z}\hat{z}} = 0, \qquad \hat{T}_{s_{\hat{z}\hat{z}}} = 0. \tag{3.65}$$

Integration of these equations and application of (3.53)–(3.56) yields

$$\hat{T} = 1, \qquad \hat{T}_s = \frac{\hat{x}}{\delta}. \tag{3.66}$$

Substitution of (3.66) into (3.57) then yields $1/\delta = \hat{S}\dot{\delta}$, whence

$$\delta = \left(\frac{2\hat{t}}{\hat{S}}\right)^{1/2}. \tag{3.67}$$

This indicates that the thickness of the solid layer in a pore will grow as $t^{1/2}$.

In order to obtain an expression for $\hat{w}$, (3.48) is integrated twice and (3.49) and (3.50) are applied:

$$\hat{w} = \frac{(\hat{x} - \delta)(\hat{x} + \delta - 2)}{2}\left[\frac{\hat{p}(\hat{z} = 0) + 2/(1 - \delta)}{h_p} + \hat{\mathscr{B}}\right]. \tag{3.68}$$

An expression for W can then be obtained from (3.68) as follows

$$\begin{aligned} W &= \frac{n}{2}\int_0^2 \hat{w}\,\mathrm{d}\hat{x} \\ &= -n\left(\frac{1}{3} + \frac{\delta^2}{2} - \delta\right)\left(\frac{p(z = 0) + 2/(1 - \delta)}{h_p} + \hat{\mathscr{B}}\right). \end{aligned} \tag{3.69}$$

This equation must be re-dimensionalized and then re-scaled using the scalings relevant in the drop region:

$$W = -K\left[\frac{1}{3} + \frac{t}{S} - \left(\frac{2t}{S}\right)^{1/2}\right]\left[\mathscr{B}\left(1 + \frac{h + h_s}{h_p}\right) - \frac{(h + h_s)_{xx} - \mathscr{C}\left[1 - (2t/S)^{1/2}\right]^{-1}}{h_p}\right], \tag{3.70}$$

where we have used continuity of pressure at $z = 0$ so that $p(z = 0) = \mathscr{B}(h + h_s) - (h + h_s)_{xx}$. In (3.70), $K \equiv nb^2 a_0^2/h_0^4$ is a dimensionless measure of the permeability, which in this case is time-dependent, and $\mathscr{C} \equiv 2a_0^2/(bh_0)$ which controls the relative significance of capillary suction through the pores.

From (3.33) and (3.70), an evolution equation for h_p can be obtained:

$$h_{p_t} = -\frac{W}{[1 - (2t/S)]\phi_0}, \tag{3.71}$$

where, as a result of the solidification process, the porosity is time-dependent and ϕ_0 is the initial porosity of the medium.

An evolution equation governing the dynamics of $h(x, t)$ can finally be obtained following the substitution of (3.60) and (3.70) into (3.11):

$$h_t - \left[\frac{h^3}{3}(\mathscr{B}(h + h_s) - (h + h_s)_{xx} - \Pi)_x\right]_x = WH(t_1 - t) - \left[1 - H(t_1 - t)\right]\mathscr{R}h_{s_t}, \tag{3.72}$$

where $t = t_1$ when $W = 0$. Thus, the end of the first stage coincides with

$$t = t_1 = 0.09S, \tag{3.73}$$

which is a function of the Stefan number only; here, we have made use of the minus sign in the root of the prefactor in (3.70). Inspection of (3.73), the suction term

Parameter	Definition	Estimate
Rescaled Hamaker constant	$\mathscr{A} \equiv \frac{a_0^2 A}{\sigma h_0} = 4/h_*$	80–800
Bond number	$\mathscr{B} \equiv \frac{\rho g a_0^2}{\sigma}$	0–10
Biot number	$B_s \equiv \frac{\alpha h_0}{\lambda}$	0.1–10
Suction number	$\mathscr{C} \equiv \frac{2a_0^2}{bh_0}$	10^3–10^6
Permeability parameter	$K \equiv \frac{nb^2 a_0^2}{h_0^4}$	0–10^{-5}
Thermal conductivity ratio	$\mathscr{L} \equiv \frac{\lambda}{\lambda_s}$	10^{-2}–100
Density ratio	$\mathscr{R} \equiv \frac{\rho_s}{\rho}$	0.8–2
Stefan number	$S \equiv \frac{\rho_s \Delta H_m \sigma h_0^5}{\mu a_0^4 \lambda_s (T_m - T_w)}$	5–10^5
Dimensionless air temperature	$\theta_a \equiv \frac{T_a - T_w}{T_m - T_w}$	0–10

TABLE 1. Dimensionless parameters appearing in (3.64), (3.70), (3.71) and (3.72) and order of magnitude estimates of their values.

of (3.70), and (3.71) reveals that no singular behaviour occurs, that is, the porosity remains finite as W approaches zero.

The dynamics of the spreading process are governed by (3.64), (3.71) and (3.72), which are coupled by (3.70). Note that in the limit $\mathscr{R} \to 0$ and $S \to \infty$, the equations studied by Alleborn & Raszillier (2004) that govern droplet spreading and imbibition on a porous substrate are recovered. Furthermore, in the additional limit of $K \to 0$, the case of droplet spreading by capillarity and gravity on an impermeable substrate is recovered (Schwartz & Eley 1998).

The physical problem described by (3.64), (3.71) and (3.72) is parametrically rich. We give the various parameters appearing in these equations in table 1, together with order of magnitude estimates of their values before turning our attention to the numerical solutions, which are discussed next.

4. Numerical solutions

In this section, we present a discussion of our results. We begin by providing details of the numerical procedure employed to carry out the computations. We then present the results of a full parametric study of the spreading and solidification process.

4.1. *Numerical procedure*

The routine used to perform the computations in the present work is EPDCOL (Keast & Muir 1991). This procedure employs finite-element collocation to discretize the spatial derivatives and uses Gear's method to advance the solutions in time. EPDCOL is a highly reliable routine, which has been used to compute solutions to interface equations in a variety of settings (see, for instance, Warner, Craster & Matar 2002*a*, *b*).

Numerical solutions of (3.64), (3.71) and (3.72) are obtained over a spatial domain of length up to two dimensionless units, $0 \leqslant x \leqslant 2$, using up to 1000 grid points. Symmetry about the drop axis was assumed and convergence was achieved upon refinement of the grid size. The solutions were obtained starting from the following initial conditions

$$h(x, 0) = \max(A_1 - A_2 x^2 + h_*, h_*), \tag{4.1}$$

$$(h_s, h_p)(x, 0) = 0.01. \tag{4.2}$$

The solutions presented in this section have $A_1 = 2$, $A_2 = 10$ and $h_* = 0.005$. Equation (4.1) represents the physical situation in which a paraboloidal mound of liquid is deposited on a solid substrate, which has been pre-wetted with a very thin precursor layer of thickness h_*. Equation (4.2) represents the initial values of the solid and saturation front in the porous medium. Their specification is necessary in order to circumvent difficulties related to singularities in (3.64) and (3.71), which are associated with having $(h_s, h_p)(x, 0) = 0$. We have, however, ensured that the numerical solutions are very weakly dependent on the exact value of $(h_s, h_p)(x, 0)$.

In order to prevent imbibition and solidification of the precursor layer, which is essential for modelling expediency, we introduce a thickness-dependent permeability parameter and Stefan number, $K(x) = \mathscr{F}K$ and $S(x) = \mathscr{F}S$, in which $\mathscr{F}$ is expressed by (Schwartz & Eley 1998; Alleborn & Raszillier 2004)

$$\mathscr{F} = \tfrac{1}{2}(1 + \tanh[10^3(h - 1.2h_*)]). \tag{4.3}$$

The function $\mathscr{F}$ reduces the value of both K and S to zero as $h \to h_*$ and recovers their original values for $h \gg h_*$. We have ensured that the numerical solutions are essentially independent of the exact form of $\mathscr{F}$, although, as will be shown in §5, the time scales for the spreading process will have to be adjusted *post facto* to achieve agreement between theory and experiment.

We have also examined the dependence of the numerical solutions on the value of the dimensionless precursor thickness, h_*. In figure 10, we show the temporal evolution of the maximal film thickness for the case of isothermal spreading of a drop on an impermeable substrate; this is characterized by $\mathscr{B} = 1$, $K = 0$ and $S \to \infty$. Inspection of the solutions shown in this plot over four decades in time reveals that they become essentially independent of the value of h_* with decreasing h_*; the solutions for $h_* = 0.01$ and $h_* = 0.005$ are very similar. The remaining plots shown in the present work have all been generated using $h_* = 0.005$ which is also the value used in the majority of the computations of Schwartz & Eley (1998) and Alleborn & Raszillier (2004). We turn our attention now to the discussion of our numerical results.

4.2. *Numerical results*

We begin the discussion of our results by examining the spreading of a droplet over a permeable substrate at high Stefan numbers. In figure 11, we show the spatio-temporal development at early times of the droplet height together with that of the saturation and solidification fronts $\mathscr{B} = B_s = \mathscr{L} = \mathscr{R} = 1$, $\mathscr{C} = 10^4$, $K = 5 \times 10^{-6}$, $S = 10^5$, $\Theta_a = 0.5$ and $\phi_0 = 0.35$. This choice of parameters dictates that, t_1, the end of the first stage of the spreading process, is $t_1 = 9000$, which implies that solidification is not expected to affect the spreading process; this is the case studied by Alleborn & Raszillier (2004). In figure 12, we show the late-time dynamics of the spreading process for the same parameters as in figure 11, while in figure 13 we plot the temporal evolution of the maximal liquid drop thickness,
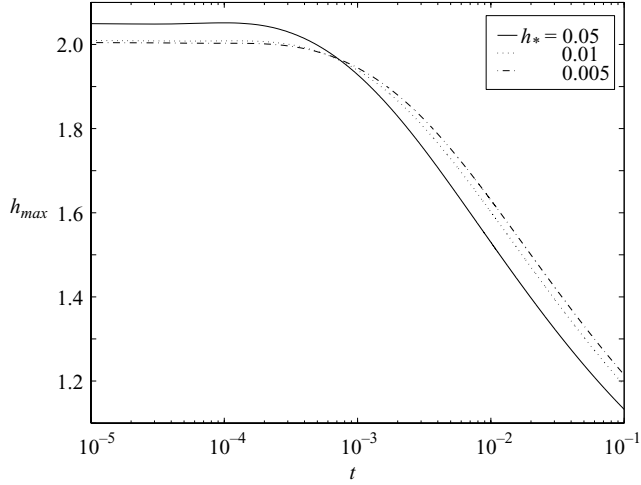
FIGURE 10. The effect of altering the dimensionless precursor film thickness, h_*, on the temporal evolution of the maximal film thickness for the case of droplet spreading on an impermeable substrate in the absence of solidification. The parameter values are $\mathscr{B} = 1$, $K = 0$ and $S \to \infty$.
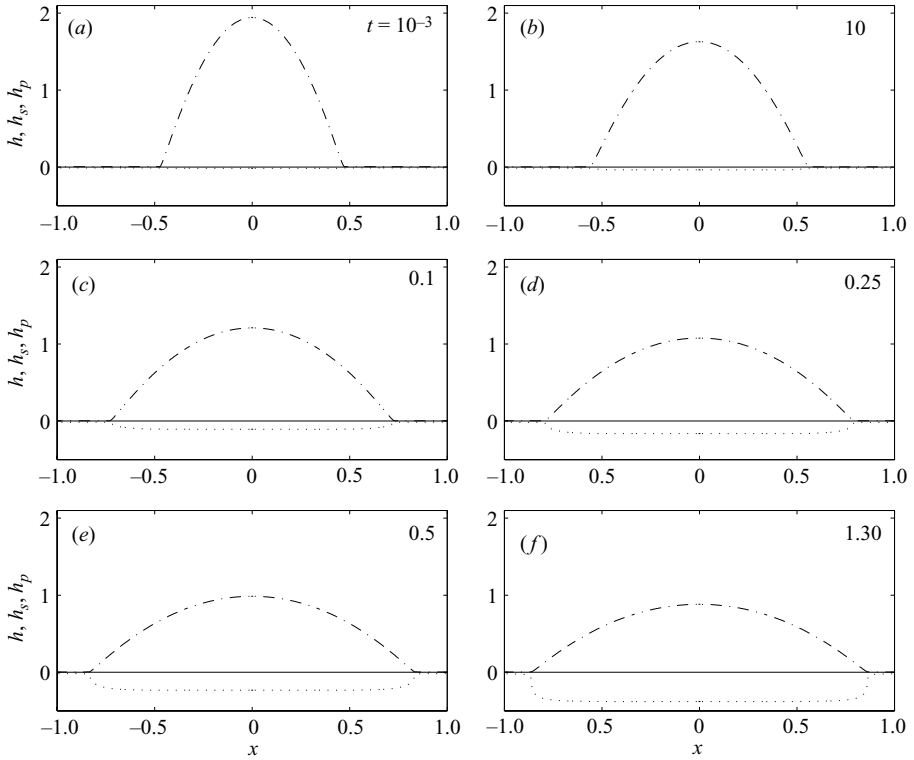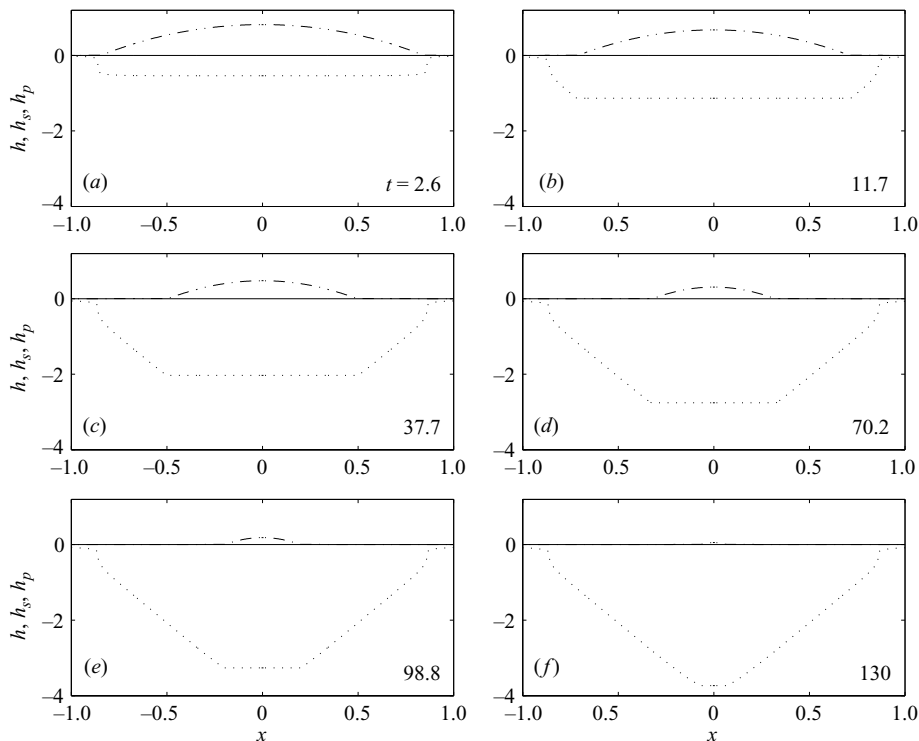

FIGURE 11. Evolution of the droplet thickness (dot-dashed lines), saturation (dotted lines) and solid (solid lines) fronts at high Stefan numbers: early-time dynamics. The parameter values are $\mathscr{B} = B_s = \mathscr{L} = \mathscr{R} = 1$, $\mathscr{C} = 10^4$, $K = 5 \times 10^{-6}$, $S = 10^5$, $\Theta_a = 0.5$ and $\phi_0 = 0.35$.

FIGURE 12. Evolution of the droplet thickness (dot-dashed lines), saturation (dotted lines) and solid (solid lines) fronts at high Stefan numbers: late-time dynamics. The parameter values are the same as in figure 11.

h_{max}, and maximal solid front, $h_{s_{max}}$, the horizontal extent of the liquid drop, x_{max}, the ratio of the apparent to equilibrium contact angles (taken to equal h_{max}/x_{max}), and the maximal vertical extent of the saturation front, $h_{p_{max}}$.

The droplet is driven to spread under the combined action of gravity and capillarity at very early times. Close inspection of figures 11(a) and 11(b) shows that very little imbibition into the porous medium has occurred, which is also evident from figure 13. At $t = 0.1$ (see figure 11c) sufficient imbibition has taken place, which gives rise to a well defined saturation front. This front grows deeper into the porous medium, as shown in figures 11(d) to 11(f), and the continued imbibition into the permeable substrate accelerates the flattening of the droplet (see also figure 13a).

In figure 12, we show the development of h, h_p and h_s at later times for the same parameter values as those used to generate figure 11. In figure 12(a) it is clearly seen that the magnitude of the droplet apparent contact angle has diminished considerably so that, as shown in figure 12(b), the droplet begins to dewet the porous substrate. This is because the apparent contact angle has decreased to a lower value than the equilibrium contact angle. This also becomes clear upon inspection of figures 13(b) and 13(c); the latter panel shows that x_{max} has reached a maximal value before decreasing with increasing time. This dewetting process continues, accompanied by continued imbibition into the porous substrate, as depicted in figure 12(c–f), which shows that the saturated front has penetrated to a considerable depth within the medium below the flow origin; the lateral extent of this front, however, has reached its maximal value at a time which coincides approximately with the onset of the
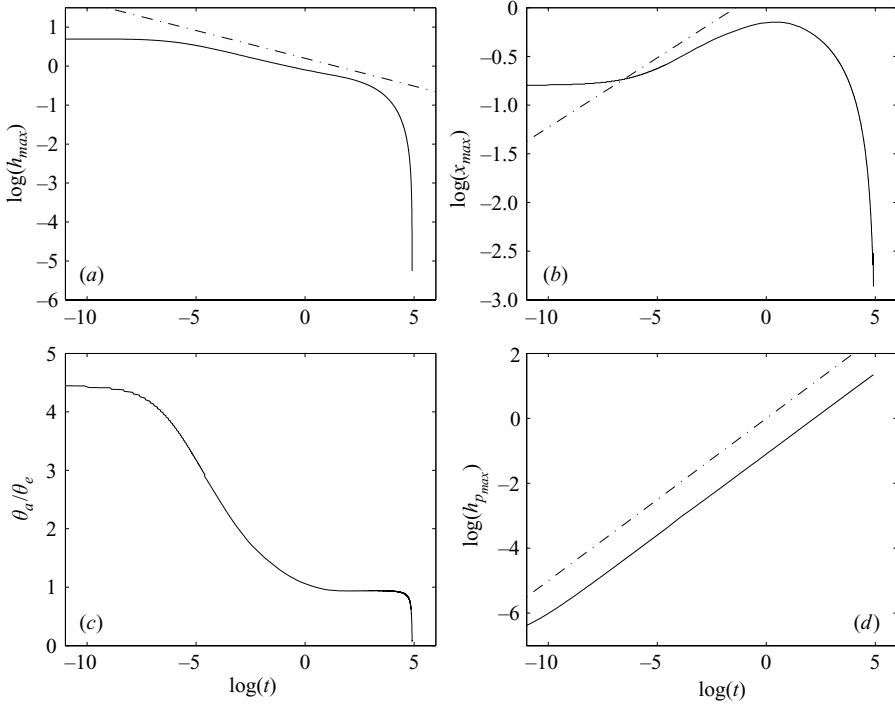
FIGURE 13. (*a*) Temporal evolution of the maximal liquid drop thickness, h_{max}, and maximal solid front, $h_{s_{max}}$, (*b*) the horizontal extent of the liquid drop, x_{max}, (*c*) the ratio of the apparent to equilibrium contact angles, and (*d*) the maximal vertical extent of the saturation front, $h_{p_{max}}$. The parameter values are the same as in figures 11 and 12. The dot-dashed lines shown in (*a*), (*b*) and (*d*) have slopes of $-1/7$, $1/7$ and $1/2$, respectively.

dewetting process. At the latest stages of the spreading, prior to the disappearance of the droplet into the porous medium, the contact angle undergoes a very rapid decrease to zero (see figure 12*f* and figure 13*a,c*). It is also worth noting that as, shown in figure 13(*a,b*), our numerical predictions are in agreement with power-law scalings for h_{max} and x_{max}, $h_{max} \sim t^{-1/7}$ and $x_{max} \sim t^{1/7}$, which are expected for capillary-driven spreading of a two-dimensional droplet over an impermeable substrate (before the onset of the imbibition-induced dewetting) (Ehrhard & Davis 1991). The numerical results are also consistent with the scalings for h_p based on the Washburn equation, which predicts that $h_p \sim t^{1/2}$ (see figure 13*d*). The results shown in figures 11 to 13 are similar to those reported by Alleborn & Raszillier (2004). Note that the solidification process, which occurs within the porous medium has a very minor effect on the dynamics, as expected, since the time scale over which the droplet has virtually disappeared, $t \approx 130$ is much smaller than t_1.

Next we examine the spreading and imbibition processes at sufficiently low values of the Stefan number so that the solidification process is expected to have a pronounced effect on the dynamics. In figure 14, we show the spatio-temporal evolution of h, h_p and h_s for $0 \leqslant t < t_1$, that is over the 'first' stage of the spreading, for the same parameter values as those used to generate figures 11 and 12 except $S = 25$ for which $t_1 = 2.25$; figures 15 and 16, respectively, show the profiles for $t > t_1$ and the temporal evolution of h_{max}, $h_{s_{max}}$, x_{max}, θ_a/θ_e and $h_{p_{max}}$. Inspection of figure 14, shows that the solutions in this case are qualitatively similar to those shown in figure 11: the droplet
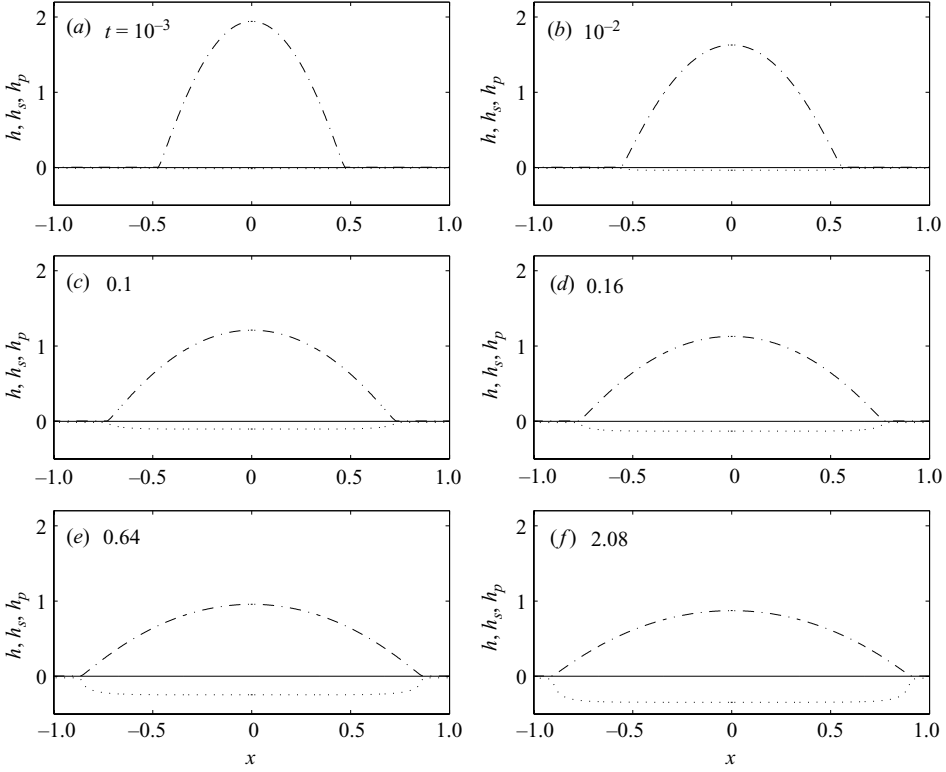
FIGURE 14. Evolution of the droplet thickness (dot-dashed lines), saturation (dotted lines) and solid (solid lines) fronts at relatively low Stefan numbers: spreading and imbibition. The parameter values are $\mathscr{B} = B_s = \mathscr{L} = \mathscr{R} = 1$, $\mathscr{C} = 10^4$, $K = 5 \times 10^{-6}$, $S = 25$, $\Theta_a = 0.5$ and $\phi_0 = 0.35$.

relaxes owing to capillary and gravitational forcing in addition to imbibition into the porous medium. This is also reflected by the solutions shown in figure 16, which are very similar to those shown in figure 13 at early times.

In figure 15, we show numerical solutions of (3.64), (3.71) and (3.72) for $t > t_1$, for which $W = 0$ owing to solidification within the pores, which causes the imbibition process to be arrested and the thickness of the saturation front to reach its maximal value; droplet solidification then takes place from below. Figure 15(a) shows the liquid droplet lying atop a solidification front which has developed near the substrate. As the solidification process continues, the size of the liquid droplet decreases and this is accompanied by steepening of the droplet at the point of 'contact' with its own solid phase (the so-called 'tri-junction') and an increase in the apparent contact angle in that region (see figure 15b–d). This can also be seen upon inspection of figure 16. In figure 16(a), the increase in $h_{s_{max}}$ is clearly seen to coincide with the sharp decrease of h_{max}, the maximal thickness of the liquid droplet. It also appears that at the later stages of the solidification process, $h_{s_{max}} \sim t^{1/2}$, which is expected to follow from (3.64) when $B_s h \ll 1$ and $Sh_{s_t} \sim 1/h_{s_t}$. In figure 16(b), it is seen that x_{max} also undergoes a sharp decrease during the solidification stage as the spatial location of the tri-junction shifts towards the flow origin. Evidence for droplet steepening can also be seen in figure 16(c), which shows a marked increase in the ratio θ_a/θ_e during solidification. The solidification culminates in the formation of a drop that exhibits
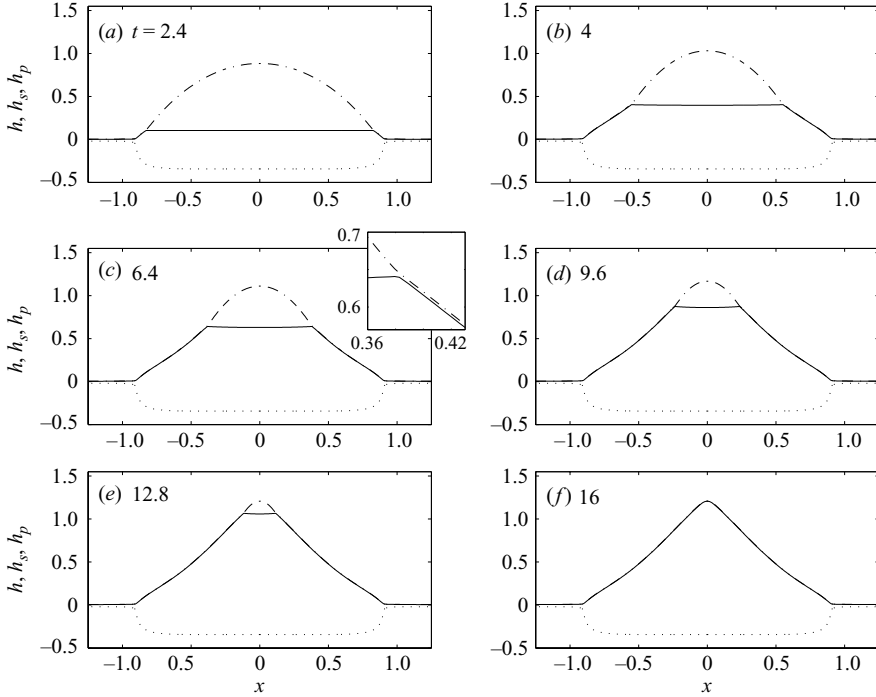
FIGURE 15. Evolution of the droplet thickness (dot-dashed lines), saturation (dotted lines) and solid (solid lines) fronts at relatively low Stefan numbers: solidification. The parameter values are the same as in figure 14. The inset in figure (c) shows an enlarged view of the 'tri-junction'; here, a very thin precursor extends out from both sides of the drop to cover the underlying solidified phase.

a point of inflection and cusp-like structure at its apex. Similar structures have been reported in the work of Anderson *et al.* (1996). Note that $h_{p_{max}} \sim t^{1/2}$ and reaches a maximal value prior to the onset of solidification beyond which it remains constant, as shown in figure 16(d).

Next, we discuss the results of a parametric study, in which we assess the effect of altering S, B_s, $\mathscr{L}$, $\mathscr{R}$ and Θ_a (see table 1 for definitions) on the spreading dynamics; the values of $\mathscr{B}$, K, $\mathscr{C}$ and ϕ_0 are kept constant. We begin by studying the effect of altering S on the temporal evolution of the maximal liquid drop thickness, h_{max}, maximal solid front, $h_{s_{max}}$, the horizontal extent of the liquid drop, x_{max}, the ratio of the apparent to equilibrium contact angles, θ_a/θ_e, and the maximal extent of the saturation front, $h_{p_{max}}$. This is shown in figure 17 for $S = 5, 25, 10^5$; the rest of the parameters are the same as in figure 14. This plot shows that decreasing S, which corresponds to a decrease in the time scale associated with the release of the latent heat of fusion to that related to conduction, lowers the onset time of solidification as shown in figure 17(a, b). The increase in the ratio θ_a/θ_e and the arrest of the imbibition process due to pore blockage also occurs earlier with decreasing S; this is shown in figures 17(c) and 17(d). In figure 18, we show the 'final' shapes of the solidified droplets for $S = 5, 25, 10^5$. Here, it is seen that decreasing the value of S results in imbibition fronts of smaller thickness and more well-rounded droplet profiles with slightly less pronounced inflection points. The reason for the latter trend is the following. If the solidification time scales are large in relation to the spreading
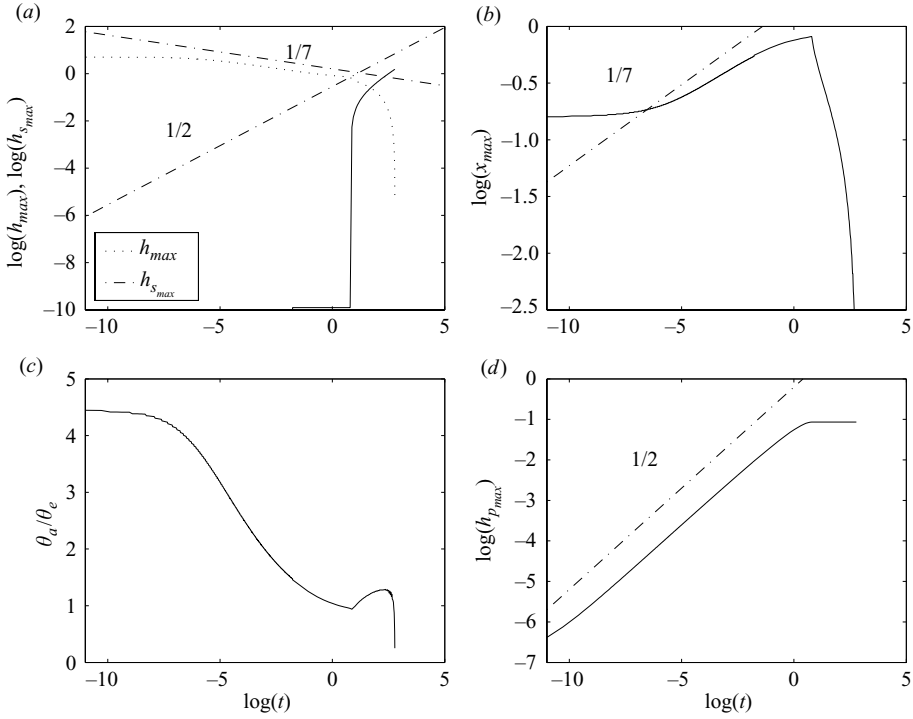
FIGURE 16. (*a*) Temporal evolution of the maximal liquid drop thickness, h_{max}, and maximal solid front, $h_{s_{max}}$ (*b*) the horizontal extent of the liquid drop, x_{max} (*c*), the ratio of the apparent to equilibrium contact angles, and (*d*) the maximal vertical extent of the saturation front, $h_{p_{max}}$. The parameter values are the same as in figures 14 and 15. The dot-dashed lines shown in (*a*) have slopes of $-1/7$ and $1/2$, while those in (*b*) and (*d*) have slopes of $1/7$ and $1/2$, respectively.

time scales (that is, for relatively large S) then basal solidification will occur at a time during which the contact angle is smaller than that at equilibrium. The combined effects of dewetting and solidification then give rise to the shapes shown in figure 6. For small S values, on the other hand, solidification occurs sufficiently early for the contact angle to be larger than its equilibrium value. Then it is possible to have spreading (rather than dewetting) accompanied by basal solidification, which gives rise to more well-rounded droplet shapes.

In figure 19, we show the effect of varying the surface Biot number, B_s, on h_{max}, $h_{s_{max}}$ and θ_a/θ_e with $B_s = 0.1, 1$ and 10 and the rest of the parameters remaining unchanged from figure 17. Note that in figure 19 we do not show plots of the temporal evolution of $h_{p_{max}}$, which, in each case, are identical to those shown in figure 17 for $B_s = 1$. Inspection of the results shown in figure 19 reveals that increasing B_s accelerates the solidification process. This is to be expected since increasing B_s reflects an increase in the rate of heat transfer from the hot droplet. Also, as shown in figure 19(*d*), the final shapes of the solidified droplets become more well-rounded with decreasing B_s although it is noted that these shapes do not appear to be highly sensitive to variations in B_s over two orders of magnitude. One can envisage, however, that B_s may become a critical parameter if interfacial crust formation had been taken into account in the present model.
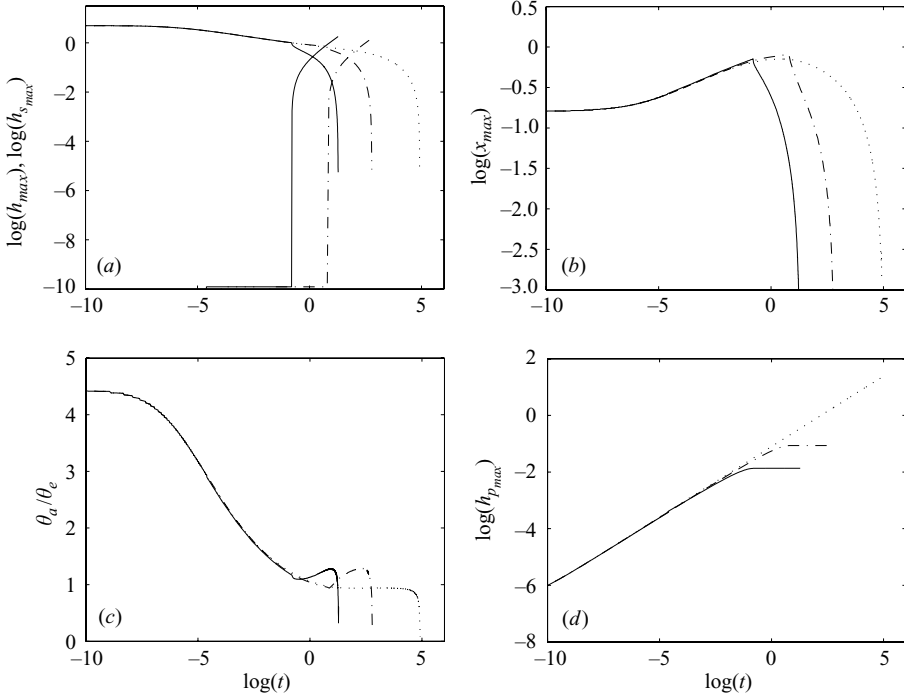
FIGURE 17. (*a*) The effect of varying the Stefan number, *S*, on the temporal variation of the maximal liquid drop thickness, h_{max}, and maximal solid front, $h_{s_{max}}$, (*b*) the horizontal extent of the liquid drop, x_{max} (*c*) the ratio of the apparent to equilibrium contact angles, and (*d*) the maximal extent of the saturation front, $h_{p_{max}}$. Here, $S = 10^5$, 25 and 5 are shown using dotted, dot-dashed and solid lines, respectively, and the rest of the parameter values remain unaltered from figure 14.
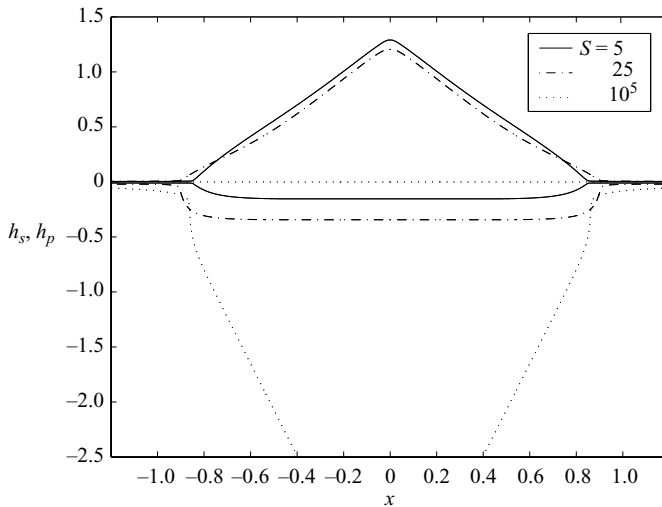

FIGURE 18. The effect of varying the Stefan number, *S*, on the final shape of the solidified droplet and saturation front profile for $S = 5, 25, 10^5$ shown at $t = 3.6, 16.15, 130$, respectively. The rest of the parameter values remain unaltered from figure 14.
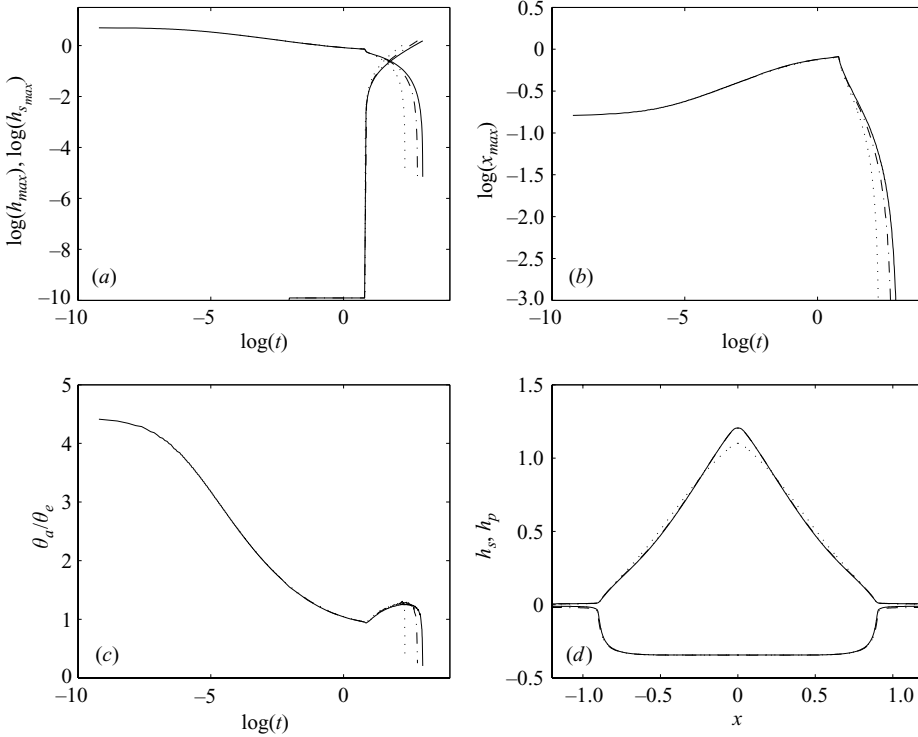
FIGURE 19. (*a*) The effect of varying the Biot number, B_s, on the temporal variation of the maximal liquid drop thickness, h_{max}, and maximal solid front, $h_{s_{max}}$, (*b*) the horizontal extent of the liquid drop, x_{max}, (*c*), the ratio of the apparent to equilibrium contact angles, and (*d*) the final shapes of the solidified drops and saturation front profiles. Here, $B_s = 0.1$, 1 and 10 are shown using dotted, dot-dashed and solid lines, respectively, and the rest of the parameter values remain unaltered from figure 17. The profiles in (*d*) are shown at $t = 19.76, 16.15, 10.1$ for $B_s = 0.1, 1, 10$, respectively; the curves associated with $B_s = 1$ and $B_s = 10$ shown in (*d*) are virtually indistinguishable.

The effect of varying the ratio of thermal conductivities, $\mathscr{L} = \lambda/\lambda_s$, on the dynamics of the spreading process was also studied. This is shown in figure 20 for $\mathscr{L} = 0.01$, 1 and 100 and the same parameter values as in figure 17. Increasing $\mathscr{L}$, which corresponds to a relative increase of the thermal conductivity of the liquid phase, λ, over that of the solid phase, λ_s, promotes droplet solidification. This is explained by the fact that smaller temperature gradients are required for the transfer of energy from the hot droplet to the cooler base as λ increases. Note that apart from affecting the onset time for droplet solidification, variation of B_s and $\mathscr{L}$ have only a minor effect on the overall shape of the θ_a/θ_e curves. Increasing $\mathscr{L}$, however, leads to the formation of final shapes of the solidified droplets with more pronounced cusp-like features at the apex (see figure 20*d*).

Next we examine the parametric dependence of the spreading dynamics on the ratio of the densities, $\mathscr{R} = \rho_s/\rho$. In figure 21, we show the temporal evolution of h_{max}, $h_{s_{max}}$, x_{max} and θ_a/θ_e for $\mathscr{R} = 0.8$, 1 and 2 and the same parameters as in figure 17. Decreasing $\mathscr{R}$, that is increasing the value of ρ in relation to ρ_s, leads to a delay in the onset of solidification and a relative increase in the ratio of θ_a/θ_e at intermediate times; this corresponds to steepening of the droplet at the tri-junction. This steepening is due to the decrease in the volume of the denser liquid drop, which is dictated by
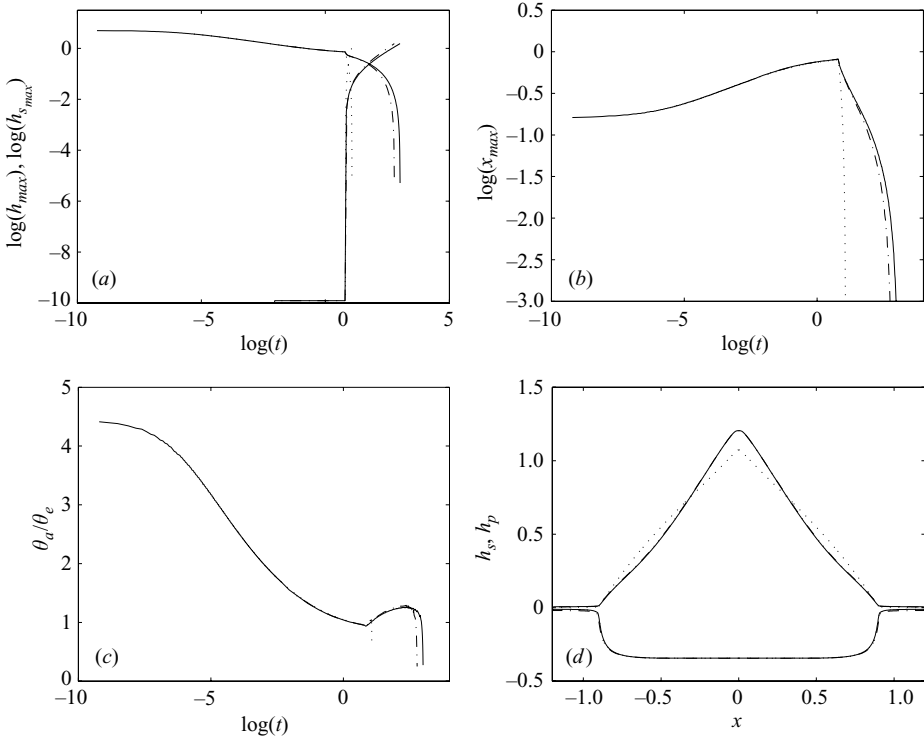
FIGURE 20. (*a*) The effect of varying the ratio of thermal conductivities, $\mathscr{L}$, on the temporal variation of the maximal liquid drop thickness, h_{max}, and maximal solid front, $h_{s_{max}}$, (*b*) the horizontal extent of the liquid drop, x_{max}, (*c*), the ratio of the apparent to equilibrium contact angles, and (*d*) the final shapes of the solidified drops and saturation front profiles. Here, $\mathscr{L} = 0.01$, 1 and 100 are shown using dotted, dot-dashed and solid lines, respectively, and the rest of the parameter values remain unaltered from figure 17. The profiles in (*d*) are shown at $t = 20.36, 16.15, 2.93$ for $\mathscr{L} = 0.01$, 1, 100, respectively.

mass conservation considerations. The delay in the onset of solidification, on the other hand, may be interpreted as being due to an effective increase of the Stefan number, which has the effect of decelerating solidification. Note that, as shown in figure 17(*d*), the ratio $\mathscr{R}$ has a marked effect on the final shapes of the solidified droplets: increasing $\mathscr{R}$ leads to larger droplets with pronounced cusp-like features, while decreasing $\mathscr{R}$ gives rise to smaller, more well-rounded droplet shapes.

Finally, we have examined the effect of varying the dimensionless air temperature on the dynamics of the spreading process for $\Theta_a = 0$, 0.5 and 1 and the same parameters as in figure 17. The results (which are not shown, but are structurally very similar to those illustrated in figure 19) indicate that increasing the value of Θ_a from zero, the case for which the substrate and surrounding air are in thermal equilibrium, delays the onset of solidification process. This is because an increase in T_a with T_w and T_m remaining fixed decreases the rate of heat transfer from the hot droplet. In fact, increasing Θ_a has the same qualitative effect as decreasing B_s and $\mathscr{L}$, as shown in figures 19 and 20. Variation of Θ_a also has a minor effect on the characteristics of the θ_a/θ_e curves and the final shapes of the solidified droplets for the parameter values investigated in the present work. We turn our attention now to the comparison between our modelling predictions and experimental data.
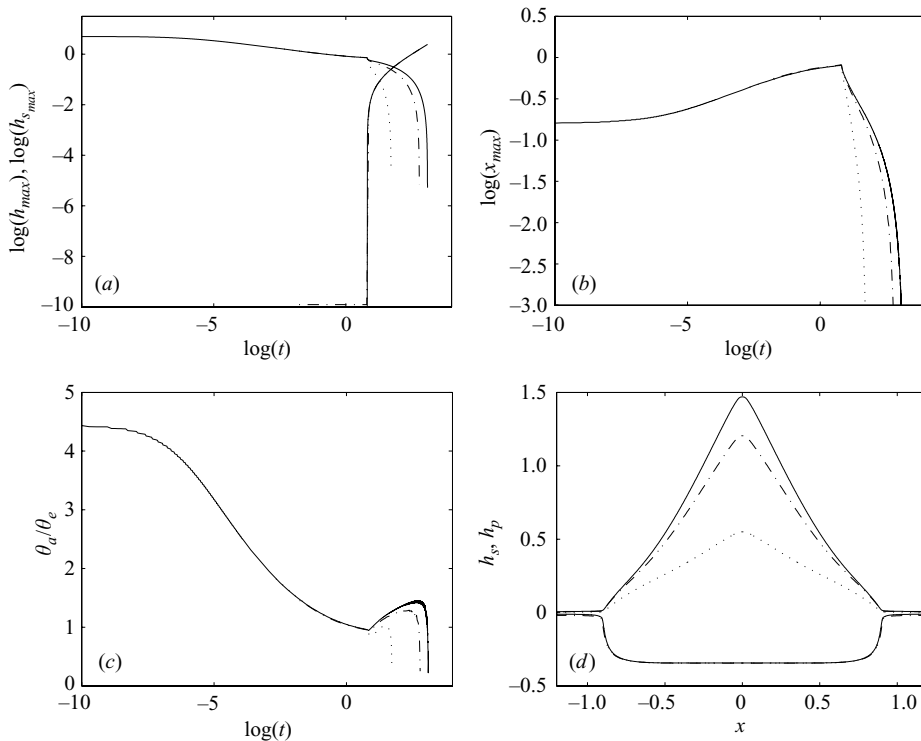
FIGURE 21. The effect of varying the ratio of solid to liquid densities, $\mathscr{R}$, on the temporal variation of the maximal liquid drop thickness, h_{max}, and maximal solid front, $h_{s_{max}}$, (a), the horizontal extent of the liquid drop, x_{max}, (b), the ratio of the apparent to equilibrium contact angles, (c), and the final shapes of the solidified drops and saturation front profiles, (d). Here, $\mathscr{R} = 0.8$, 1 and 2 are shown using dotted, dot-dashed and solid lines, respectively, and the rest of the parameter values remain unaltered from figure 17. The profiles in (d) are shown at $t = 22.03, 16.15, 5.54$ for $\mathscr{R} = 0.85$, 1, 2, respectively.

5. Comparison between theory and experiment, and model limitations

Here, we attempt to validate our model by comparing its predictions with experimental data. We show in figure 22 a comparison of the predicted and measured variation of the dimensionless droplet base diameter with time. (Here, this quantity represents the ratio of the droplet diameter at a given time to that at the onset of the spreading process.) The experimental data chosen for this comparison correspond to the curves labelled '1'–'4' in figure 5. The initial droplet volume and radius in each case are approximately equal to 15 mm^3 and 1.92 mm, respectively. The characteristic height and length scales were estimated to be $h_0 = 0.93$ mm and $a_0 = 4.47$ mm from the equilibrium shape of a PEG1500 droplet spreading on a nearly impermeable substrate. This was made from the same material (sodium carbonate) as the tablets discussed in the previous section, but using a higher pressure (12 Mt) to compress the particles that had diameters approximately equal to 75 μm. Using these values, curves 1–4 are then characterized by the following dimensionless parameters $\mathscr{B} = 4.81$, $B_s = 0.06$, $\mathscr{C} = 1712$, $K = 6.39 \times 10^{-6}$, $\mathscr{L} = 1.04$, $\mathscr{R} = 1.08$, $\Theta_a = 0$ and $\phi_0 = 0.35$. Moreover, curves 1–4 are distinguished by different Stefan numbers, which are equal to $S = 21.7, 65.2, 97.5$ and ∞, respectively; the latter value corresponds to the case in which no solidification is possible since $T_s > T_m$. The initial condition for the droplet,
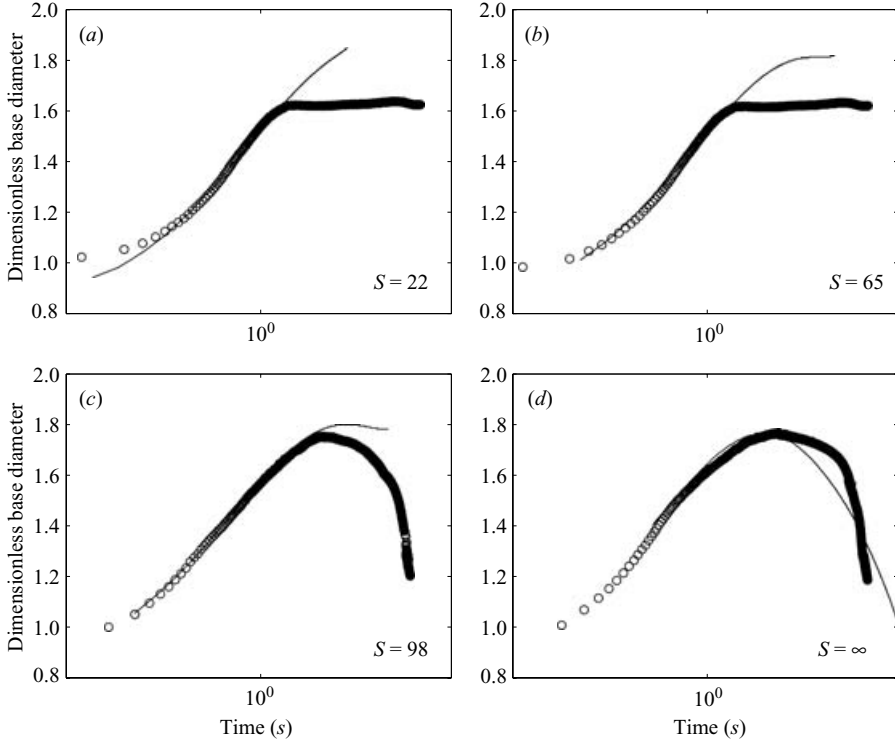
FIGURE 22. Comparison of modelling predictions (solid lines) with experimentally obtained data (circles) for the temporal evolution of the basal radius.

which is necessary for the numerical computations corresponds to a paraboloidal shape characterized by $A_1 = 1.7$ and $A_2 = -9$ in (3.1), which has the same volume as that of the droplets used in the experiments; (3.2) was used as an initial condition for h_s and h_p and $h_* = 0.005$ was fixed in all of the computations.

Inspection of figure 22 shows that the agreement between the model predictions and experimental data is reasonably good. The dynamics are predicted well during the earlier stages of the spreading process, but the maximal dimensionless basal diameter is over-predicted by the model for curves 1 and 2 in which solidification occurs. It should be noted, however, that because of our use of the precursor-layer model with $h_* = 0.005$, the spreading rate was over-predicted. Thus in order to correct for this, we have multiplied our time scales by a factor of 2.5, which is in line with the value of 2.8 that was previously determined by Schwartz & Eley (1998) following the reduction of h_* by two orders of magnitude.

It is also noteworthy that the experimental results shown in figure 7 are reminiscent of those discussed in § 4 (see, for instance, figures 18, 19d and 20d although it should be noted that these results were generated for the case of spreading on a permeable substrate). Note also that as shown in figure 21, the ratio of solid to fluid densities has a significant effect on the final shapes of solidifying droplets. In fact, the final shape of the solidified droplet shown in figure 7(f), which is characterized by a ratio approximately equal to 0.9, is very similar to those shown in figure 21(d) for a ratio of 0.8 and 1.

In view of these results, it is important to highlight the shortcomings and limitations of the model adopted in the present work. (i) A precursor layer model was adopted

in order to relieve potential numerical problems associated with the contact line singularity and the specification of a slip law in that region in order to advance the droplet. This introduced an extra parameter into the problem, namely the dimensionless precursor layer thickness, h_*. A similar approach to the one adopted here, however, has previously been followed in the literature by Schwartz & Eley (1998) and Alleborn & Raszillier (2004). These studies have shown that the calculated flow profiles become essentially independent of h_* for sufficiently small values of h_*. This was also demonstrated in the present paper in figure 10; however, adjustments to the time scales became necessary when establishing a direct comparison between experimental observations and modelling predictions.

(ii) The problem formulation associated with the porous medium assumed the substrate to be of uniform porosity, being composed of pores of uniform width and length, which, of course, represents an idealization. Moreover, the flow within the porous medium was taken to be one-dimensional which is another idealization. Future work should perhaps remove these from the mathematical description of the problem in order to generate more sophisticated predictive models.

(iii) The heat transfer problem solved within the drop and the substrate had a number of limitations. These included the assumption that the porous medium is infinitely conducting and that its temperature remained constant throughout all the stages of the spreading, imbibition and solidification processes. The limitations also included the assumption that the Péclet numbers within the solid and melt phases are very small. In certain situations such as lava flows (Balmforth & Craster 2000; Balmforth *et al.* 2004), the Péclet numbers may be relatively large. Future models should therefore also examine the situation in which thermal convection is important, which may lead to even more interesting dynamics.

(iv) The physical properties of both the solid and melt phases, such as the densities, melt viscosity, thermal conductivities and surface tension, have all been assumed to be temperature-independent. These effects may be important, particularly those associated with temperature-dependent viscosities, as noted by previous authors (Sakimoto & Zuber 1995; Bercovici & Lin 1996; Balmforth & Craster 2000; Bunk & King 2003), and should therefore be incorporated into future models.

(v) The present model assumes that the droplet undergoes basal solidification at the beginning of the second stage of the dynamics; this, of course, precludes the possibility of simultaneous crust formation (and 'buckling' shown in figures 3 and 4 in §2) via cooling of the air–melt interface. Accounting for this potential feature of the dynamics would give rise to a more complicated model owing to the necessary presence of an extra interface corresponding to the upper solid–melt interface. Nevertheless, this feature must be incorporated into future models in order to provide more accurate predictions of the dynamics and faithful representation of physically realizable situations.

Note, finally, that the results presented are for the case of a two-dimensional rather than an axisymmetric droplet, which would perhaps have been more appropriate from a physical standpoint.

6. Conclusions

We have investigated the dynamics of spreading, imbibition and solidification of a two-dimensional droplet bounded from above by air on a porous substrate composed of an array of pores having constant width. Lubrication theory was used to derive evolution equations for the droplet thickness and heights of the saturation front in

the porous medium and of the sharp solid–melt interface within the drop by assuming the Péclet numbers within the drop and porous medium to be small; a precursor layer and a disjoining pressure model were used to relieve the contact line singularity at the edge of the droplet. The evolution equations are parameterized by a relatively large number of dimensionless groups, reflecting the relative importance of permeability, capillary suction in the porous medium, heat transfer and solidification, in addition to gravity, capillarity at the droplet free surface, and intermolecular forces. Numerical solutions of the model equations were obtained using a reliable numerical routine based on the finite-element method over a wide range of parameters. The spreading dynamics of PEG melts on porous sodium carbonate substrates were also investigated experimentally using a commercially available droplet-shape analyser.

The results of our numerical parametric study have indicated that the dynamics depend critically on the time scales which characterize spreading, imbibition and solidification. For a given value of the permeability parameter, spreading of the droplet and its imbibition into the porous medium is accompanied by solidification within the medium. This solidification eventually leads to blockage of the pores on a time scale governed by the Stefan number, S, a ratio of the rates of release of the heat of fusion and conduction. Following the end of this stage of the dynamics, the droplet undergoes basal solidification, which, depending on the value of S and other parameters such as the ratio of solid to liquid densities, thermal conductivies, and surface Biot number, can result in final solidified droplet shapes that exhibit cusp-like features at the droplet apex. A comparison of modelling predictions with experimental observations, performed in terms of the temporal evolution of the droplet basal radius, revealed reasonably good agreement and highlighted the limitations of the present model.

Future work will focus on the derivation of more sophisticated models that are valid for large Péclet numbers and which do not preclude simultaneous basal solidification and crust-formation at the air–liquid interface.

REFERENCES

Acton, J. M., Huppert, H. E. & Worster, M. G. 2001 Two-dimensional viscous gravity currents flowing over a deep porous medium. *J. Fluid Mech.* **440**, 359–380.

Alleborn, N. & Raszillier, H. 2004 Spreading and sorption of a droplet on a porous substrate. *Chem. Engng Sci.* **59**, 2071–2088.

Anderson, D. M., Worster, M. G. & Davis, S. H. 1996 The case for a dynamic contact angle in containerless solidification. *J. Crystal Growth* **163**, 329–338.

Aradian, A., Raphael, E. & de Gennes, P. G. 2000 Dewetting on porous media with aspiration. *Eur. Phys. J.* E **2**, 367–376.

Balmforth, N. J. & Craster, R. V. 2000 Dynamics of cooling domes of viscoplastic fluid. *J. Fluid Mech.* **422**, 225–248.

Balmforth, N. J., Craster, R. V. & Sassi, R. 2004 Dynamics of cooling viscoplastic domes. *J. Fluid Mech.* **499**, 149–182.

Baral, D., Hutter, K. & Greve, R. 2001 Asymptotic theories of large-scale motion, temperature and moisture distribution in land-based polythermal ice sheets. A critical review and new developments. *Appl. Mech. Rev.* **54**, 215–256.

Bercovici, D. & Lin, J. 1996 A gravity current model of cooling mantle plume heads with temperature-dependent buoyancy and viscosity. *J. Geophys. Red. Solid. Earth* **101**, 3291–3309.

BUNK, M. A. 1999 *Modellierung zur Ausbreitung von Schmelzen bei gleichzeitiger Erstarung*. PhD thesis, University of Karlsruhe, Germany.

BUNK, M. A. & KING, J. R. 2003 Spreading melts with basal solidification. *Z. Angew. Math. Mech.* **83**, 820–843.

CLARKE, A., BLAKE, T. D., CARRUTHERS, K. & WOODWARD, A. 2002 Spreading and imbibition of liquid droplets on porous surfaces. *Langmuir* **18**, 2980–2984.

DAVIS, S. H. & HOCKING, L. M. 1999 Spreading and imbibition of viscous liquid on a porous base. *Phys. Fluids* **11**, 48–57.

DAVIS, S. H. & HOCKING, L. M. 2000 Spreading and imbibition of viscous liquid on a porous base. ii. *Phys. Fluids* **12**, 1646–1655.

DENESUK, M., SMITH, G. L., ZELINSKI, B. J. J., KREIDL, N. J. & UHLMANN, D. R. 1993 Capillary penetration of liquid droplets into porous materials. *J. Colloid Interface Sci.* **158**, 114–120.

EHRHARD, P. & DAVIS, S. H. 1991 Non-isothermal spreading of liquid drops on horizontal plates. *J. Fluid Mech.* **229**, 365–388.

GREVE, R. 1997 Large-scale ice-sheet modelling as a new means of dating deep ice cores in Greenland. *J. Glaciol.* **43**, 307–310.

GRIFFITHS, R. W. 2000 The dynamics of lava flows. *Annu. Rev. Fluid Mech.* **32**, 477–518.

HOLMAN, R. K., CIMA, M. J., UHLAND, S. A. & SACHS, E. 2002 Spreading and infiltration of inkjet-printed polymer solution droplets on a porous substrate. *J. Colloid Interface Sci.* **249**, 432–440.

KEAST, P. & MUIR, P. H. 1991 Algorithm 688 EPDCOL – a more efficient PDECOL code. *ACM Trans. Math. Software* **17**, 153–166.

KING, J., RILEY, D. & SANSOM, A. 2000 Gravity currents with temperature-dependent viscosity. *Comput. Assist. Mech. Engng Sci.* **7**, 251–277.

MYERS, T., CHARPIN, J. & CHAPMAN, S. J. 2002 The flow and solidifiction of a thin fluid film on an arbitrary three-dimensional surface. *Phys. Fluids* **14**, 2788–2803.

ORON, A., DAVIS, S. H. & BANKOFF, S. G. 1997 Long-scale evolution of thin liquid films. *Rev. Mod. Phys.* **69**, 931.

SAKIMOTO, S. E. H. & ZUBER, M. T. 1995 The spreading of variable-viscosity axisymmetric radial gravity currents: applications to the emplacement of Venusian 'pancake' domes. *J. Fluid Mech.* **301**, 65–77.

SCHWARTZ, L. W. & ELEY, R. R. 1998 Simulation of droplet motion on low-energy and heterogeneous surfaces. *J. Colloid Interface Sci.* **202**, 173–188.

SIMPSON, J. 1997 *Gravity Currents*. Cambridge University Press.

STAROV, V. M., KOSTVINTSEV, S. R., SOBOLEV, V. D., VELARDE, M. G. & ZHDANOV, S. A. 2002*a* Spreading of liquid drops over saturated porous layers. *J. Colloid Interface Sci.* **246**, 372–379.

STAROV, V. M., VELARDE, M. G. & ZHDANOV, S. A. 2002*b* Spreaing of liquid drops over dry porous layers: complete wetting case. *J. Colloid Interface Sci.* **252**, 397–408.

STAROV, V. M., ZHDANOV, S. A. & VELARDE, M. G. 2002*c* Spreading of liquid drops over thick porous layers: complete wetting case. *Langmuir* **18**, 9744–9750.

SUNDERHAUF, G., RASZILLIER, H. & DURST, F. 1999 Levelling behaviour of a particle containing liquid evaporating on a porous surface. In *Advances in Coating and Drying of Thin Films: Third European Coating Symposium* (ed. H. Raszillier & F. Durst), pp. 163–168. Shaker.

TANNER, L. M. 1979 Spreading of silicone oil drops on horizontal surfaces. *J. Phys.* D **12**, 1473.

TEUNOU, E. & PONCELET, D. 2002 Batch and continuous fluid bed coating: review and state of the art. *J. Food Engng* **53**, 325–340.

WARNER, M. R. E., CRASTER, R. V. & MATAR, O. K. 2002*a* Dewetting of ultrathin surfactant covered films. *Phys. Fluids* **14**, 4040.

WARNER, M. R. E., CRASTER, R. V. & MATAR, O. K. 2002*b* Unstable van der Waals driven line rupture in Marangoni driven thin viscous films. *Phys. Fluids* **14**, 1642.

WARREN, P. B. 2004 Late stage kinetics for various wicking and spreading problems. *Phys. Rev.* E. **69**, 041601.

WASHBURN, F. W. 1921 The dynamics of capillary flow. *Phys. Rev.* **17**, 273.